Available online at www.sciencedirect.com
SCIENCE DIRECT
Coordination Chemistry Reviews 250 (2006) 730–754
COORDINATION CHEMISTRY REVIEWS
www.elsevier.com/locate/ccr

Review

Actinide speciation using X-ray absorption fine structure spectroscopy

Melissa A. Denecke *

Forschungzentrum Karlsruhe, Institut für Nukleare Entsorgung, PO Box 3640, D-76021 Karlsruhe, Germany

Received 11 July 2005; accepted 19 September 2005
Available online 25 October 2005

Contents

Abstract

Actinide speciation by means of X-ray absorption fine structure (XAFS) is reviewed with emphasis on actinide speciation in the field of nuclear disposal safety research. The XAFS method, both experimental and theoretical aspects, is concisely presented. Numerous examples of recent research results of actinide speciation using XAFS are discussed. In addition to illustrating important aspects of research dealing with nuclear waste disposal safety, the examples also contain basic and advanced aspects of the XAFS technique, as well as strategies for data evaluation.

Keywords: EXAFS; XANES; Actinides; Nuclear waste disposal

1. Introduction

One of the key concerns in the safe disposal of high level nuclear waste is the possibility for radionuclides to leach out of a waste form, breach the repositories multi-barrier system and enter the surrounding environment (see Fig. 1,

* Tel.: +49 7247 825536; fax: +49 7247 823927.
E-mail address: melissa@ine.fzk.de.

0010-8545/$ – see front matter © 2005 Elsevier B.V. All rights reserved.
doi:10.1016/j.ccr.2005.09.004

Nomenclature

ANL	Argonne National Laboratory
APS	Advanced Photon Source
d	sample thickness or beam path length
d	crystal plane spacing
DCM	double crystal monochromator
DFT	density functional theory
E and $h\nu$	photon energy
EXAFS	extended X-ray absorption fine structure
E_{kin}	photoelectron kinetic energy
E_0	ionization energy
$f(k)$	backscattering amplitude function
FT	Fourier transform
GI	grazing incidence
$\hbar$	Plank's constant, reduced
HA and FA	humic acid and fulvic acid
INE	Institut für Nukleare Entsorgung
I_0	incident photon intensity
I_1	transmitted photon intensity
JAERI	Japan Atomic Energy Research Institute
k	photoelectron wave vector
k_{bn}	beat node k-value
ℓ	angular momentum quantum number
LC	loading capacity
LIBD	laser induced breakdown detection
m_e	electron mass
M	atomic weight
MARS	MAtière Radioactive à Soleil
MC	Monte Carlo
MS	multiple scattering
$(n\text{-}C_3H_7)_4$-BTP	2,6-di(5,6-dipropyl-1,2,4-triazin-3-yl)pyridine
N	coordination number
NEXAFS	near edge X-ray absorption fine structure
N_{free}	number of allowed free variables in data modeling
P and T	partitioning and transmutation
PCA	principle component analysis
R	interatomic distance between absorber and backscatterer
ROBL	Rossendorfer BeamLine
SLS	Swiss Light Source
SR	synchrotron radiation
SS	single scattering
STXM	scanning transmission X-ray microscopy
S_0^2	amplitude reduction factor
TRLFS	time-resolved laser fluorescence spectroscopy
WL	white line
XAFS	X-ray absorption fine structure
XANES	X-ray absorption near edge structure
XRF	X-ray fluorescence

Greek symbols

ε	polarization vector
Θ	Bragg angle of reflection
Θ_i	incident angle
λ	wavelength
$\lambda(k)$	photoelectron mean free path length
μ	absorption coefficient
μ_0	absorption coefficient of an isolated atom
σ^2	mean square average displacement
$\Phi(k,R)$	total phase shift
$\chi(k)$	EXAFS function

top). Predicting or ultimately controlling or prohibiting the transport of released radionuclides through the environment requires a detailed understanding of the physical and chemical factors and processes determinant in their transport. Of central importance is the radionuclide speciation, or its molecular, chemical and physical form. The radionuclide speciation determines transport properties (mobilization/immobilization), reactivity, bioavailability and, hence, its potential human and environmental risk. Due to the fact that the long-lived

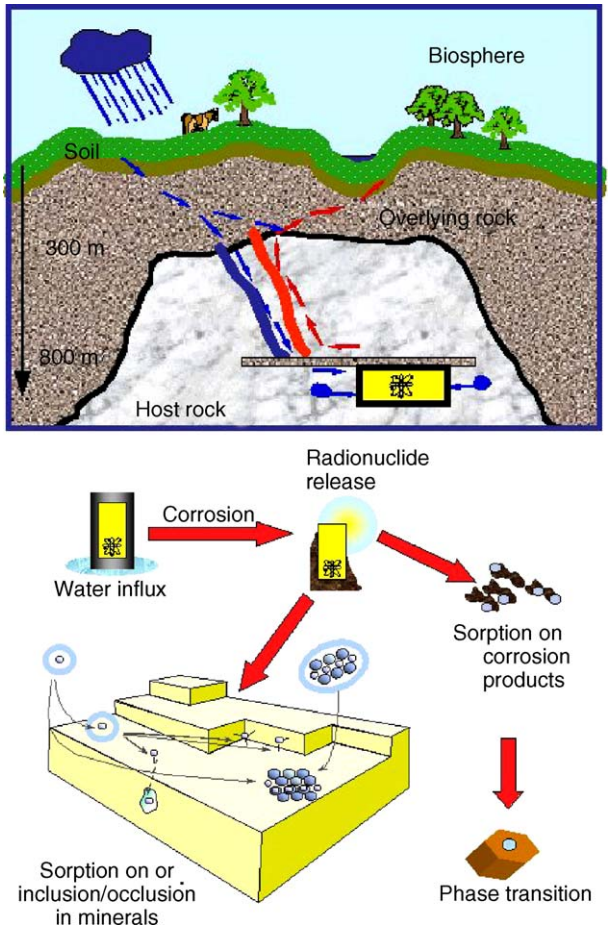

Fig. 1. (Top) Schematic representation of a repository for high level nuclear waste in a deep geological formation. The worst case scenario of water entering the repository and transporting radioactive contaminants out of the repository and to the biosphere is indicated. (Bottom) Schematic representation of some possible fates of radionuclides released from a repository following water intrusion and corrosion of the waste package. See text for details.

actinide elements make the major long-term contribution to the radiotoxicity of a nuclear repository, nuclear waste disposal safety speciation investigations concentrate on the actinides.

X-ray scattering and spectroscopic techniques are extremely useful speciation methods. In fact, the application of synchrotron radiation based techniques in actinide science has experienced a boom over the past decade (see, e.g., [1–4]). The reasons for this increased activity are manifold. The driving force is the real need for molecular-scale actinide speciation information. Of additional importance is the increasing sophistication of the available tools, including ever increasing brilliance delivered by machines, advances in focusing methods and increasing sensitivity/resolution of detectors. This growing sophistication is helping meet the challenges faced by nuclear waste disposal safety speciation investigations, including the high chemical and physical heterogeneity of the matrices involved (waste form, containers, back-fill, bedrock, ground water, to name a few) and the localization of many reactions/processes at junctions or interfaces (e.g., ground water–mineral interface).

To illustrate these points, a schematic representation of the processes that can play a role in the fate of an actinide cation released from a nuclear waste repository is shown in Fig. 1 (bottom). Following water intrusion into the repository and corrosion of the waste package, radionuclide contaminants can be released. The number of factors potentially influencing radionuclide fate are immense and the complexity of the problem is enormous. For example, the radionuclide can sorb onto the waste container corrosion products. These radionuclide-corrosion product associations can be small enough to form mobile colloids, which can be transported in the ground water. Under different chemical conditions, they can also precipitate out and/or transform to secondary mineral phases, thereby becoming immobilized. The released radionuclide can also remain dissolved as a solution species in, e.g., pore and ground waters as an aquo ion, coordinated with only water molecules. It can also remain dissolved in the form of polynuclear hydrolysis species or complexed with organic and inorganic ligands. Complexation is directly linked to the amount and type of ligands present, which, in turn, is dependent on numerous factors such as the surrounding biological activity, interchange with pedologic reactions of the surrounding back-fill, bedrock and overlying rock, the physicochemical conditions, etc. The radionuclide may sorb onto mineral surfaces in various ways, shown schematically in Fig. 1. It can "physisorb" onto the mineral through van der Waals forces, thereby forming outer-sphere complexes, or "chemisorb" forming monodentate, bidentate, or tridentate complexes on the surface. Eventually such surface species may become occluded into the mineral phase or form a solid solution with the mineral. A myriad of materials other than minerals can serve as solid sorbents, e.g., cement, ground water colloids, microorganism cell walls, plant roots or debris, etc. Other examples of processes and conditions determining radionuclide speciation include reduction or oxidation or other catalyzed transformations mediated by organic material, the prevailing redox potential, microorganisms, colloids and/or surrounding minerals.

1.1. Spectroscopic speciation studies for performance assessment of nuclear waste disposal

The above discussion of the fate of radionuclide released from a nuclear waste repository is by no means comprehensive. The important point is that whatever speciation form the nuclide takes on has a profound influence on its solubility, mobility, bioavailability, toxicity, and hence risk. For this reason, radionuclide speciation on a molecular scale is prerequisite to any safety assessment of a proposed repository.

In this review actinide speciation on a molecular scale by means of X-ray absorption fine structure (XAFS) is presented. We begin with a sort discourse of the method, including the physical origin of the spectra, experimental aspects and, as we are dealing with actinides, a discussion of available synchrotron facilities for working with radioactive material. In the remaining portion selected examples of actinide speciation in the field of nuclear disposal safety research performed at our institute by means of XAFS are presented. A summary of pedagogic aspects meant for the reader to become acquainted with in this review is in Section 3 and is intended as a self-check. If the reader recognizes these, I consider this endeavor a successful one.

1.2. X-ray absorption fine structure – XAFS

The basics of the XAFS method, including both general and actinide-specific experimental aspects, are described in the rest of Section 1. This description is intended as a general overview of the experimental method, theory, and data analysis. The reader is referred to other, partially very recent reviews, that have appeared in the literature for details [5–8].

1.2.1. General concepts

X-rays are absorbed by matter primarily through the photoelectric effect, whereby at energies above the ionization threshold electrons from inner core states are excited into empty outer-lying states. Fig. 2 depicts a typical X-ray absorption spectrum, where the product of the absorption coefficient and the sample thickness, μd, as a function of photon energy is shown for UO_2, recorded at the U L3 edge. A sharp rise or edge is observed at the absorbing element core state threshold or ionization energy, E_0, in this case *U*, which renders this technique element specific. According to the principle quantum number of the electron being excited, these abrupt changes are referred to as *K*, *L*, *M*, etc. absorption edges. A listing of absorption edge energies for the early actinide elements is given in Table 1A.

Evident in Fig. 2 is the oscillatory structure of μ. Based on the scattering processes responsible for the oscillatory structure, the photon energy range in an X-ray absorption spectrum is generally divided into two parts: the X-ray absorption near edge structure (XANES) at lower energies and the extended X-ray absorption fine structure (EXAFS) at higher energies.

In the EXAFS region, the wave function of the excited photoelectron in the core region is modulated by interference of the outgoing wave function with a fraction which has been backscattered on the neighboring atoms. In this sense the EXAFS oscillatory pattern is quite literally an interferrogram of the atomic

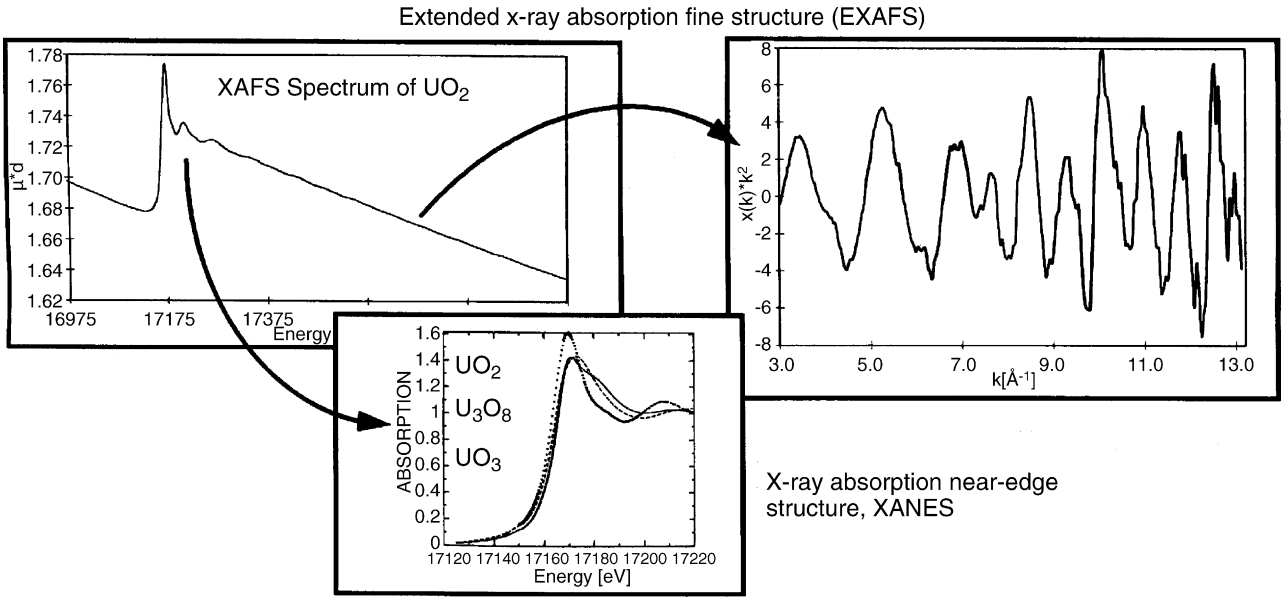

Fig. 2. Raw data U L3 edge XAFS spectrum of UO_2(s). The k^3-weighted EXAFS extracted from the raw data (right) and the normalized, background subtracted XANES (bottom), compared to that for U_3O_8 and UO_3.

arrangement surrounding the absorbing atoms. It therefore contains metrical parameters characterizing this arrangement such as number and type of neighboring atoms and their distance to the absorbing atom.

The XANES region is sometimes itself divided into two parts: the pre-edge region at energies below E_0 and the XANES region extending from the threshold to energies 50–100 eV above it. Pre-edge structures result from transitions of the photoelectron into bound excited states of the absorbing atom. For the L edges of actinides, the pre-edge region is void of structure. As in the EXAFS regime, the changes in μ within the XANES region also result from scattering of the excited photoelectron on the outlying, neighboring atoms. We shall see (Section 1.2.5), the photoelectron is not simply backscattered but undergoes multiple-scattering (MS) on the outlying atoms.

1.2.2. Facilities at synchrotron laboratories dedicated to work on radioactive samples

The number of synchrotron facilities around the world, where the infrastructure for working with radioactive materials is available, is few. Of the 23 countries having or building synchrotron facilities, only Germany, Switzerland, USA, Japan, and France either have or are planning on having dedicated facilities for performing XAFS experiments on radioactive materials. These are

Table 1
(A) Absorption edge energies (E) and (B) selected fluorescence emission line energies (E_{fl}) for the early actinide elements in eV for the transitions KL_3 ($K\alpha_1$), KL_2 ($K\alpha_2$), L_1M_3 ($L\beta_3$), L_2M_4 ($L\beta_1$), L_2N_4 ($L\gamma_1$), and L_3M_5 ($L\alpha_1$), data are from [146]

Element	E (K)	E (L_1)	E (L_2)	E (L_3)
A				
Th	109648	20470	19691	16300
Pa	112598	21100	20314	16733
U	115596	21756	20946	17165
Np	118689	22438	21615	17608
Pu	121790	23112	22270	18060
Am	124986	23808	22952	18056
Cm	128241	24515	23651	18510

Element	E_{fl} ($K\alpha_1$)	E_{fl} ($K\alpha_2$)	E_{fl} ($L\beta_3$)	E_{fl} ($L\beta_1$)	E_{fl} ($L\gamma_1$)	E_{fl} ($L\alpha_1$)
B						
Th	93347.4	89957.0	16423.9	16201.5	18978.2	12967.9
Pa	95866.4	92283.5	16930.5	16702.0	19568.5	13290.8
U	98433.8	94652.8	17455.2	17220.2	20167.3	13614.8
Np	101056.3	97068.4	17989.3	17750.4	20785.0	13944.3
Pu	103734.1	99523.2	18540.5	18294.0	21417.5	14278.7
Am	106471.3	102030.3	19106.2	18852.2	22065.4	14617.3
Cm	109272.3	104590.3	19686.9	19425.2	22732.4	14959.9

- The MARS Beamline ("MAtière Radioactive à Soleil") at Soleil, Gif-sur-Yvette, France [9].
- ROBL ("ROssendorfer BeamLine"; usable energy range 5–35 keV), at the European Synchrotron Radiation Facility, Grenoble, France [10].
- Two beamlines dedicated to actinide research BL22XU and BL23XU have been built and operated by JAERI (Japan Atomic Energy Research Institute) at SPring-8, Harima, Japan. These beamlines, however, are not for X-ray absorption spectroscopy. Such experiments can be done at BL11XU, a non-dedicated JAERI Beamline. (Usable energy range is given as 6–70 keV but U K edge XANES at 116 keV have been reported [11].)
- The Actinide Facility for Synchrotron Research in Molecular and Environmental Sciences operated by the Chemistry Division at Argonne National Laboratory (ANL), Argonne, IL, USA is not a dedicated facility. Instead the Actinide Facility provides researchers access to hot-laboratory facilities for sample manipulation before and after experiments at the Advanced Photon Source (APS) on the ANL site. They also provide needed safety and experimental equipment.
- The microXAS Beamline X05L at the Swiss Light Source (SLS) on the Paul Scherrer Institute site in Villingen, Switzerland [12]. Useable energy range 5–20 keV.
- The INE-Beamline ("Institut für Nukleare Entsorgung"-Beamline, useable energy range 2.3–23 keV) for actinide research at the ANKA facility located at the Forschungszentrum Karlsruhe, Leopoldshafen, Germany [13].
- Beamline 11-2 at the Stanford Synchrotron Radiation Laboratory (SSRL), Menlo Park, California is a facility essentially dedicated to environmental and radioactive XAFS. Useable energy range 4.5–37 keV.

1.2.3. Experimental set-up and data reduction

A generic experimental set-up of the optics and instrumentation used in a XAFS experiment is shown in Fig. 3. Synchrotron radiation from an electron or positron storage ring is used as the light source. Synchrotron radiation is emitted from centripetally accelerated charged particles (see [14] for an overview). It is a very intense, highly collimated, polarized beam of electromagnetic radiation having a continuous band of wavelengths from around the μm (infrared) to the pm (hard X-ray) range. A monochromator is used to select and vary the wavelength (λ) around the E_0 of the element of interest. The incoming synchrotron beam is diffracted on the crystal planes of the monochromator material. The energy of the exiting photons is according to the Bragg law of diffraction

$$n\lambda = 2d \sin \Theta, \qquad n = 1, 2, 3, \ldots \tag{1}$$

where d is the spacing between diffracting planes. Monochromator crystal pairs available, e.g., at the INE-Beamline for actinide research at the synchrotron source ANKA [13] are Si⟨1 1 1⟩ (d = 3.135 Å), Si⟨3 1 1⟩ (d = 1.638 Å), Ge⟨2 2 0⟩ (d = 2.000 Å), and Ge⟨4 2 2⟩ (d = 1.155 Å). By varying the angle of reflection, Θ, photon energies are selected. The photon energy in keV is related to λ in Å by

$$E\,(\text{keV}) = 12.398/\lambda\,(\text{Å}) \tag{2}$$

Most commonly one uses a double crystal monochromator (DCM). This keeps the beam propagating in the same direction following two reflections and has the advantage of suppressing higher harmonic reflections (n > 1 in Eq. (1)) by detuning slightly the parallel alignment of the crystal pair. To offset the vertical movement of the beam as Θ is varied, either the sample is moved simultaneously vertically or the second crystal is translated during the movement to maintain a fixed beam exit height.

To record a spectrum, the photon intensity in front of the sample (I_0) and behind the sample (I_1) are measured at specified energies. The absorption for a given sample length (d) is given by Lambert–Beer law

$$\mu(E)\mathrm{d} = \ln[I_0(E)/I_1(E)] \tag{3}$$

The absorption of a reference with known E_0, placed upstream from the sample, and measured simultaneously (ln[$I_1(E)/I_2(E)$])

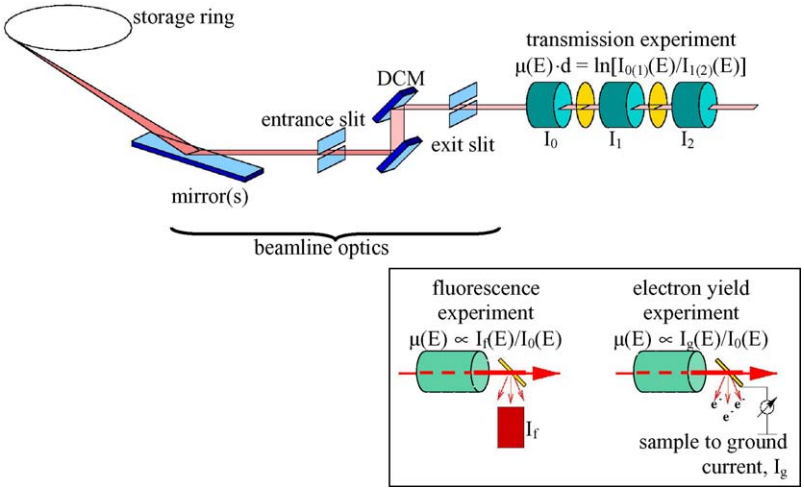

Fig. 3. Sketch of a generic X-ray absorption experiment using synchrotron radiation and standard transmission geometry. Insert at left: schematic representation of fluorescence and total electron yield methods of detection.

is used for energy calibration. For the actinide L3 edges useful references are a Y or a Zr foil with an E_0 of 17.038 and 17.998 keV, respectively [15].

In addition to registering the transmission of photon intensities, one can detect proportional secondary processes, which occur when atoms relax following inner-shell electron excitation by the X-rays such as fluorescence photon emission or emission of secondary electrons. The detection schemes for these processes are shown schematically in Fig. 3. One disadvantage of electron yield detection for actinide speciation studies related to nuclear disposal safety is that it cannot be used for aqueous or wet samples. Its advantage is that it is inherently surface specific. Fluorescence detection is required for dilute samples, i.e., where the actinide concentration (or more generally the element of interest) is less than around 1%, and for samples which are totally absorbing or impermeable for X-rays. The energies of selected fluorescence emission lines for elements Th to Cm are given in Table 1B. In the fluorescent mode of detection, the sample is rotated 45° to the incident beam direction, in the plane of the storage ring orbit, with the detector mounted at 90° to the incident beam, in order to minimize elastic and Compton scattering radiation noise reaching the detector. Note that in fluorescence detection for solid samples interference from diffracted beams, leading to large spikes in the data, can occur.

The XANES spectrum and EXAFS oscillations must be isolated from the raw XAFS data prior to analysis. For both spectral regions, XANES and EXAFS, the initial steps in the data reduction are the same: background subtraction and normalization of the edge jump to unity. For extraction of EXAFS isolations, first the energy axis is converted to photoelectron wave vector (k) values:

$$k = \sqrt{\frac{2m_e}{\hbar^2} E_{kin}}, \quad E_{kin} = (E - E_0) \tag{4}$$

where m_e is the mass of an electron and $\hbar$ the Plank's constant divided by 2π. E_{kin} is the kinetic energy of the photoelectron and is the difference between the incident X-ray energy and E_0. To calculate k, one must therefore define E_0. The problem in defining E_0 is that errors in its position are coupled to errors in determining bond distances from fits of the experimental EXAFS to the EXAFS equation (see next section). What is usually done to avoid this is to define E_0 as an easily identifiable feature in the spectrum and then treat E_0 as an adjustable parameter in the fit procedure. For the L3 X-ray absorption edges of the actinide elements, it is very practical to define E_0 as the energy of the intensity maximum of the most prominent feature in the XANES, the white line (WL), as this value is easily determined. The next steps in EXAFS data reduction (isolation of oscillation with spline polynomial fit, k-weighting, and Fourier transformation) are covered in Section 1.2.5.

1.2.4. Sample preparation and containment

The way that a sample is prepared and contained for measurement depends on the sample, its activity, the type of experiment to be performed, and the rules to be adhered to at the particular facility where the experiments are to be performed. The number of layers of containment required varies, depending on the classification of sample radiation hazard-levels, based on their activity and form.

One necessarily wants to prepare homogeneous samples for a standard XAFS experiment. For liquid samples this is simple and samples are usually put into sealed containers as primary containment vessels such as capped vials or specialized sealed containers, having windows for incident and transmitted beam, and a specified or variable volume to obtain the desired sample path length (d, see Eq. (3)). The actinide concentration ([An]) in the sample determines the optimal d. A jump in absorption across the ionization edge of unity is generally sufficient to avoid thickness effects [16]. For an edge jump of one an optimal [An] is given by $(d\,\Delta\mu\,M)^{-1}$, where $\Delta\mu$ is the change in total cross-section across the edge (around 65–50 cm^2/g for the L3 edges of Th to Cm; a X-ray cross-section database can be found on the Internet [17]) and M is the actinide atomic weight. Note that this formula does not account for absorption of the liquid matrix or other absorbing components in the sample. For relatively high beam energies, and hence penetrating photons, of K and L edges for the actinides, however, absorption of the matrix usually does not present any difficulties for transmission measurements. An example of a liquid sample cell is given in Ref. [18]. The sample cell used for the soft X-ray spectroscopic investigations presented in Section 2.2.2 is described in [19]. Paste-like samples are usually put into an appropriate vial, which is sealed for both containment purposes and to prevent drying. Solid samples are generally finely ground and either prepared neat as a thin layer between two adhesive polycarbonate, Mylar, or similar tapes or dispersed in a dilutant such as polyethylene, Teflon, or boron nitride powder and pressed into pellets. The pellet itself is often hermetically sealed in plastic foil or wrapped in adhesive tape as a containment barrier. The amount of substance (m) needed for an edge jump of one for a pressed tablet is dependent on the pellet area (A) and $\Delta\mu$: $m = A/\Delta\mu$. Due to the inherent radiation hazards involved, solid sample preparation work on transuranium element containing samples should be performed in appropriate glove boxes. Inert-atmosphere glove boxes can be used to prepare air-sensitive samples and glove boxes with adjustable CO_2 partial pressures for CO_2-sensitive solutions where necessary.

The vials/holders or solid samples wrapped in tape or sealed in foil represents the primary containment barrier. If a secondary layer of containment is necessary, the primary containment can be hermetically sealed in an additional layer of foil or can be placed into special durable holders having windows for incident, transmitted and fluorescence beams. Such holders are often designed to also serve as transport containers, or provide specialized sample environments, and/or are equipped to accommodate a number of samples. An example of a multiple-sample holder provided by the Actinide Facility is found at [20]. The technically simplest method if more containment barriers around the sample are required, is to put more than one layer of foil around the primary. For liquid samples it is wise and sometimes required to place a suitable tray or pan underneath the sample for added safety. Note that the outermost barrier for a radioactive sample in a synchrotron experiment is the experimental hutch itself. At the INE-Beamline and the ROBL stations (and planned at

MARS), the beamline experimental hutch is operated as a controlled active actinide laboratory, providing a high level of safety.

As a rule, prior to making any proposal for a XAFS experiment using radioactive samples, one should contact the beamline responsible, the radiation protection officer of the facility, or both. The required information with details of the samples themselves and the experiments planned varies between facilities, and the beamline responsible and/or the radiation protection officer will provide you with all necessary information. Experiments on samples containing natural or depleted uranium or thorium can often be performed without special authorization, as they do not present any particular radiation safety hazard, provided their presence is reported to the facility and the samples are contained in such a way as to ensure their integrity during the experiment. Experiments on transuranium elements require special authorization as a rule. In addition to sample transport and containment requirements, additional requirements such as specialized training for experimenters may be effective. The beamline responsible and/or facility radiation protection officer can inform you of the requirements. Classification of sample radiation hazard-levels is not internationally uniform. The classification will determine number of layers of containment needed and the protocol and procedures required during the experiment. These issues should be cleared before preparing the samples themselves. The reader can find good introductory information concerning experimental procedures and safety considerations for working with radionuclides at synchrotron sources in Ref. [1].

1.2.5. EXAFS: extended X-ray absorption fine structure

We have seen that the EXAFS oscillatory pattern is an interferrogram of the atomic arrangement surrounding the absorbing atom. The EXAFS function ($\chi(k)$) expresses the modulation of μ by scattering on the surrounding atoms, normalized to the absorption coefficient of an isolated atom of the absorbing atom type (μ_0) as a function of k:

$$\chi(k) = \frac{\mu - \mu_0}{\mu_0} \tag{5}$$

μ_0 is generally not known so that μ_0 is approximated by fitting an appropriate function to the smooth part of the EXAFS (often splined polynomial functions) and using this function then to calculate $\chi(k)$ according to Eq. (5). The isolated $\chi(k)$ should oscillate uniformly about the zero axis. $\chi(k)$ is often weighted with k^n, with $n = 1$–3. This accents the oscillations at higher k, where they are considerably dampened (particularly of low Z elements).

The EXAFS interference processes are schematically illustrated in Fig. 4. Constructive interference between the outgoing photoelectron wave function and backscattered wave leads to maxima in the EXAFS oscillations, destructive interference corresponds to minima. At the photon energy $h\nu_1$ the relationship between the wavelength of the photoelectron kinetic energy and the distance between the absorbing atom and the backscattering atom (R) is such that they interfere constructively. At a somewhat lower energy, $h\nu_2$, the wavelength is too long to fulfill this condition and destructive interference with the backscattered wave occurs. One intuitively predicts that the relationship between R and λ for constructive interference is periodically fulfilled and this is indeed the case. Under the assumption that the photoelectron can be approximated by a plane wave and that the sample has a minimum of disorder, the EXAFS equation is given by:

$$\chi(k) = \frac{S_0^2}{k}\ell^{-1}\sum_{j=1}^{n} N_j |f_j(k,\pi)| \frac{e^{-2R_j/\lambda(k)}}{R_j^2} e^{-2k^2\sigma^2} \times \sin(2kR_j + \Phi_j(k,R)) \tag{6}$$

where N is the coordination number; $f(k)$ the backscattering amplitude function for the neighboring atom type; $\Phi(k,R)$ the total phase shift of the photoelectron; S_0^2 the amplitude reduction factor accounting for multi-electron shake-up and shake-off effects; ℓ the angular momentum quantum number; σ^2 the mean square average displacement from the mean bond length, and $\lambda(k)$ the mean free path length of the photoelectron.

The sum in Eq. (6) is over each coordination shell j up to the nth coordination shell typically up to distances of 5 Å. Eq. (6) has essentially two terms, a phase term, $\sin(2kR + \Phi(k,R))$, and remaining amplitude term. The functions $f(k)$ and $\Phi(k,R)$ are unknown and must either be extracted empirically using EXAFS data from model compounds of known structure or theoretically calculated. $\Phi(k,R)$ is dependent on the type of neighboring atoms, as the photoelectron experiences a phase shift both as it passes through the potential of the absorbing atom and back and as is passes through the potential of the neighboring backscattering atom. That $\Phi(k,R)$ and $f(k)$ are dependent on backscatterer type allows identification of elements comprising a coordination shell from EXAFS analysis. This is true providing the types of atoms differ sufficiently in atomic number (Z). Neighboring atoms have similar functions and it is not possible to differentiate between $Z+1$ types of atoms. In Section 2.5.1 an example

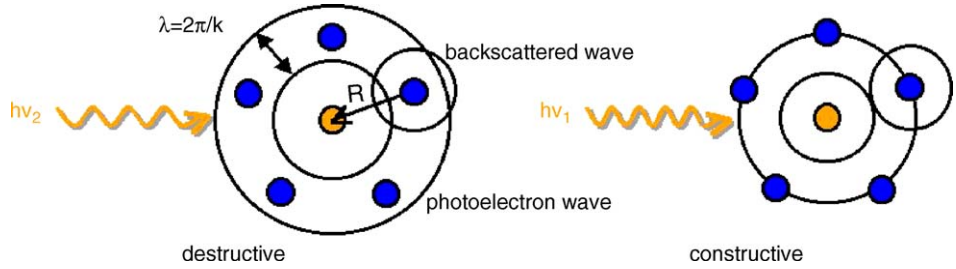

Fig. 4. Illustration of destructive and constructive interference of outgoing photoelectron wave and backscattered wave, which lead to minima and maxima of the oscillations in μ observed in the EXAFS regime.

is given where coordinating ligand C and N atoms, which are $Z+1$ types of atoms, cannot be differentiated.

By fitting experimental data to the EXAFS equation (Eq. (6)) using iterative least square fit techniques, the metrical parameters describing the coordination structure of the absorbing atom can be obtained. Values for R can be obtained with an accuracy of ± 0.02 Å. The parameters associated with the amplitude of $\chi(k)$ are obtained with less accuracy, to within about 20–25%. This is due to the large number of parameters contributing to the EXAFS amplitude and their being correlated with one another. In addition, if one is not careful a number of systematic errors can contribute to the inaccuracy of amplitude measurement. These include thickness effects from concentrated samples [16], self-absorption effects in fluorescence experiments [21], deadtime effects in fluorescence measurements, radiation leaks in or around a sample [22], contamination of I_0 with higher harmonics in the beam [22], overfitting of the polynomial spline function to μ_0, to name a few.

In the derivation of the standard EXAFS (Eq. (6)) it is assumed that the displacement of the atoms about their lattice sites can be described by harmonic oscillations. The term $\exp(-2k^2\sigma^2)$ is insufficient to describe systems without a symmetric Gaussian distribution of neighbors about the absorbing atom. In this case, additional terms modifying both amplitude and phase are needed to describe the pair distribution [23]. For systems where the disorder is too great to be described using extra terms, the amount of information obtainable from EXAFS is limited [24].

The EXAFS oscillations are a sum of contributions from n coordination shells. In order to separate the individual contribution, Fourier-filtering techniques are used. By performing a Fourier transformation from wave (k) space into real (R) space, the scattering from each distance (j-shell of atoms) is resolved into a band of Fourier coefficients along the R axis. The magnitude of the transform is a modified radial pair distribution function with peaks corresponding to scattering from atoms located at each coordination shell. The Fourier transform (FT) peaks appear at distances shorter than R_j due to the $\Phi(k,R)$ phase shift, typically around 0.5 Å shorter. The FT peaks are also broadened mostly due to limited transformation range of the data and limited instrumental resolution. Individual contributions to $\chi(k)$ can be separated using an inverse Fourier transformation. For this, selected regions in R-space are transformed back into k-space. One may, for example, isolate the functions $f(k)$ and $\Phi(k,R)$ for a given atom type from Fourier-filtered data of model compounds to use in iterative least squares fits to EXAFS data for samples of unknown coordination structure. Note that for the actinyl cations, the first two coordination shells (the two axial oxygen atoms and the atoms in the equatorial plane) are so close that they are not separable with Fourier-filtering techniques using the data range typically available (bond length resolution $\approx \pi/2k_{max}$, k_{max} the k-range available). One must, in these cases, use theoretically calculated $f(k)$ and $\Phi(k,R)$ functions. It is good practice to test the theoretically calculated functions on a compound of known structure prior to using them for fits to an unknown.

A number of ab initio programs are available for calculating theoretical $f(k)$ and $\Phi(k,R)$ functions, as well as calculating XAFS spectra. The FEFF code, named after the $f(k)$ function itself (FEFF = $f_{eff}(k)$, notation for effective curved-wave scattering amplitude) [25–27]. Feff is interfaced to the code available for analyzing EXAFS data in the UWXAFS program packages [28], FEFFIT, and to the interactive FEFFIT version IFEFFIT [29]. Other codes for calculating theoretical $f(k)$ and/or $\Phi(k,R)$ functions with interfaces to data reduction software and fit software are EXCURVE [30,31], where EXCURV98 is the most recent version, and GNXAS [32–34]. Other codes available for data analysis without a direct interface to own theoretical calculations include WinXAS [35], EXAFSPAK [36], and EXAFS pour le MAC [37].

1.2.6. XANES: X-ray absorption near edge structure

The fine structures in the XANES spectral region are also due to electron scattering processes. At lower energies near E_0 the outgoing photoelectron is not simply backscattered on the outlying neighboring atoms, but is scattered in all directions. This is because the $f(k)$ function for photoelectrons with low E_{kin} has significant values at all angles, and not only at 0°. The probability that scattering of the excited electron at all angles to occur at these energies is high. This fact, in combination with the longer $\lambda(k)$ at these same energies, leads to MS of the outgoing photoelectron. Where the E_{kin} of the photoelectron is great enough to escape the atomic potential of the central absorbing atom, it is scattered or ricocheted on a neighboring atom at some angle other than 0° in the direction of another near-neighbor atom, where it is again scattered. This process is repeated until the photoelectron eventually returns to the absorbing atom.

It is the MS character of XANES that renders this method sensitive to multi-atom correlation functions, i.e., the XANES region contains information about the coordination geometry of the absorbing atom, including interatomic distances and angles. However, this information is not easily extracted from XANES data. XANES features and their intensity and energy position are observed to be dependent on a number of factors in addition to just coordination geometry and interatomic distances. These factors include absorbing atom valence, orbital occupancy, electronegativity of coordinating atoms, and orientation of anisotropic samples. Because the XANES features depend on more parameters than the EXAFS, its theoretical treatment has lagged behind. There is no simple XANES equation, such as exists for the EXAFS region (Eq. (6)). One finds generally two strategies to interpret XANES spectra. One is comparison of observed features in unknowns with XANES features of known compounds. This is often referred to as 'fingerprinting'. The other strategy involves performing theoretical XANES calculations under variation of specified parameters such as sample orientation or atomic cluster size to explain observed trends in experimental data. In two sections we will discuss examples of using fingerprints for understanding the interaction of natural organic acids acting as complexing agents for actinide cations: Section 2.2 in our discussion of S K XANES and Section 2.2.2, where we will turn to an example in the soft X-ray regime of C 1s XANES fingerprinting (often referred to as near edge X-ray absorption fine structure or NEXAFS in the soft X-ray region instead of XANES).

Because the XANES region involves transitions about E_0, the valence state of the absorbing atom can also be determined from XANES data. In Fig. 2 we see that the edge shifts towards higher energies in the order UO_2, U_3O_8, UO_3 due to reduced shielding of the core electrons (i.e., increase in E_0 of the core electrons) associated with the increase in mean valence state across the series. By comparing XANES edge energies of samples with known oxidation states with that of an unknown, the oxidation of the unknown can be identified. The reader is referred to further examples of XANES measurements of actinide elements in different oxidation state in the literature (see [38,39] for Np [40–43] for Pu, and [44] for Bk). This method has the particular advantage as determinations can be performed in situ, without prior separation or drying procedures, which might alter the metal (actinide) cation oxidation state. Oxidation state determinations, including quantification of valence mixtures through linear combination of XANES spectra from reference compounds, is straightforward for systems where XANES structure and corresponding energy position between oxidation states are very different. Valence determinations of the actinide elements is a particular challenge as some of their various oxidation states exhibit modest L3,2 edge XANES differences. The formation of short actinide–oxygen bonds in actinyl cations for the (V) and (VI) oxidation states leads to characteristic MS XANES features, which can be used for their identification. At the same time, this complicates valence determinations especially in mixtures as the (V) states exhibit WL energies relative to their (IV) counterparts, which are in the reverse order as expected [39]. Furthermore, the intensity of the most prominent XANES WL feature is observed to vary not only with the valence, but also with the degree of condensation of the sample phase [45,46].

To illustrate these points, we now turn to the example of redox speciation of Pu. The redox chemistry of Pu is complex. Plutonium can be present in four oxidation states, (III)–(VI), in natural aqueous samples (see Fig. 5). One or more oxidation states can be present at the same time [47]. XANES spectra for Pu in its (III)–(VI) valence states are depicted in Fig. 6. All

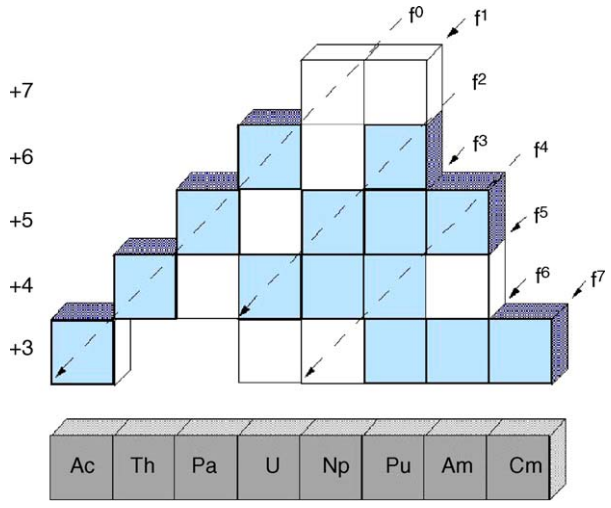

Fig. 5. Known oxidation states for the actinide elements Ac to Cm (indicated at left) and their corresponding f-electron configuration (indicated at right). The oxidation states stable in natural environments are highlighted.

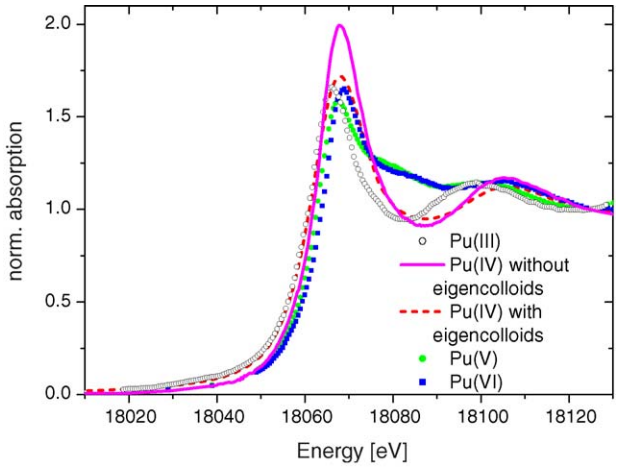

Fig. 6. Pu L3 edge XANES for aqueous solutions of Pu in various oxidation states.

spectra are calibrated relative to the first inflection point in the Zr K XANES for a Zr foil with energy 17.998 keV [15]. Table 2 lists values for the energy position for the WL maxima and the position of the inflection points at the rising edge, determined as the first maximum in first derivative spectra. Also listed are the energy differences between the various valence states relative to Pu(III). All values are given in eV. The energy position of the XANES WL for Pu(IV) appears more than 1 eV above that for Pu(V). Normally an increase in E_0 with increasing valence state of the absorbing atom is observed; this is not the case for the XANES features for tetravalent and pentavalent actinide cations. Comparison of WL intensities in Fig. 6 shows that Pu(IV) has a larger WL than the plutonyl cations, Pu(V) and Pu(VI). In addition to their lower WL intensity, another distinguishing feature in the Pu(V) and Pu(VI) spectra is the MS resonance at the high energy flank of the WL, about 15 eV above the WL. This MS XANES feature is characteristic for L3,2 edge XANES of "yl" cations [48], resulting from scattering along the axial oxygen atoms (O*ax*) of the linear actinyl moiety [49]. The energy position of this MS feature depends greatly on the actual actinyl–O*ax* bond distance [50]. This MS feature is missing in the Pu(III) and Pu(IV) spectra. The appearance of the MS feature can be used for identifying the presence of actinyl cations. However, this MS feature is not easily discernible in XANES of valence state mixtures so that it not being present in the XANES does not rule out the presence of minor amounts of actinyl species. That

Table 2
Energy positions of the white line (WL) maxima, inflection points, and shifts relative to Pu(III) for the XANES spectra in Fig. 6

Sample	WL maximum	Inflection point	Δ-Energy[a]	Δ-Energy[b]
Pu(III)	18066.0	18062.0	0.0	0.0
Pu(IV) aquo species	18067.9	18064.0	1.9	1.9
Pu(IV) eigencolloids	18068.1	18062.3	2.1	0.2
Pu(V)	18067.6	18062.7	1.6	0.7
Pu(VI)	18068.8	18065.7	2.8	3.6

[a] Relative to Pu(III) WL.
[b] Relative to Pu(III) inflection point.

the WL intensity also varies with the degree of condensation of the sample can be seen in the two Pu(IV) spectra. The partially hydrolyzed Pu(IV) solution containing eigencolloids (dashed line in Fig. 6) exhibits a less intense WL than that of the Pu(IV) aquo ion solution spectrum without colloids (solid line). This difference in WL intensity leads to a shift in the energy position of the inflection point, whereas the position of the WL maximum shows no significant change. Such intensity differences can lead to errors in quantitative determinations of valence mixtures.

1.2.7. Multiple scattering in the EXAFS regime

In addition to single scattering (SS) of the photoelectron from the absorbing atom to the neighboring atoms and back presented in Section 1.2.4, oscillations from MS of the photoelectron can also play a role in the EXAFS regime. This is especially true for MS paths along atoms with a collinear arrangement. An unusually large EXAFS amplitude for atoms is observed, which have intermediate atoms lying between it and the absorber at angles near 180°. This is often referred to as a "lensing" or "focusing" effect. Such focusing MS occurs because the $f(k)$ function has significant probability for scattering of the excited electron in the forward direction (180°), in addition to 0°.

An example illustrating these points that one encounters in natural systems is MS to the distal oxygen (O*dis*) via the intermediate C atom for bidentate coordinated carbonate ligands. The distance between U and O*dis* in the aqueous tricarbonato uranium(VI) anion complex $UO_2(CO_3)_3^{4-}$ is over 4 Å and one would not expect to observe EXAFS at room temperature for such a poor backscattering light atom. This, however, is not the case [51–53]. The FT peak for the O*dis* atoms is clearly visible at ΔR near 3.7 Å in the U L3 EXAFS for an aqueous $UO_2(CO_3)_3^{4-}$ solution (45.5 mM HCO_3^-, 45.5 mM CO_3^{2-}, and 9.09 mM UO_2^{2+}; $-\log H_c = 9.6$) shown in Fig. 7. Also shown in this figure is a theoretically calculated EXAFS using the structural model shown at top, right. In order to correctly model the $UO_2(CO_3)_3^{4-}$ spectrum, MS must be included. Path analysis reveals the three-legged MS path U → C → O*dis* → U to be responsible for the 'triplet' structure in the EXAFS between k 6.5 and 8.5 $Å^{-1}$. Note that the effective path length (R_{eff}) for a MS path is equal to one-half of the sum of the path distances involved. In this case, R_{eff} is the same as R(U–O*dis*) so that the EXAFS amplitude for these O*dis* atoms is increased over that expected for simple SS. The analysis of the MS paths has been used to determine the number of coordinating carbonate ligands in Th(IV) mixed hydroxo carbonate species [54,55], in pentacarbonato U(IV), Np(IV), and Pu(IV) complexes present in aqueous solutions in approximately 1 M $KHCO_3$ ([56–58], respectively) or even higher carbonate concentrations [59]. Note that a similar focusing effect for the O*dis* via an intermediate N atom for bidentate coordinated nitrato ligands is also expected.

A special MS case of focusing MS paths observed in actinide L3,2 EXAFS is MS along linear actinyl cations $[Oax = An^{n+} = Oax]^{(4-n)+}$, $n = 5$ or 6. The importance of the four-legged (An → O*ax* → An → O*ax* → An) MS path was first

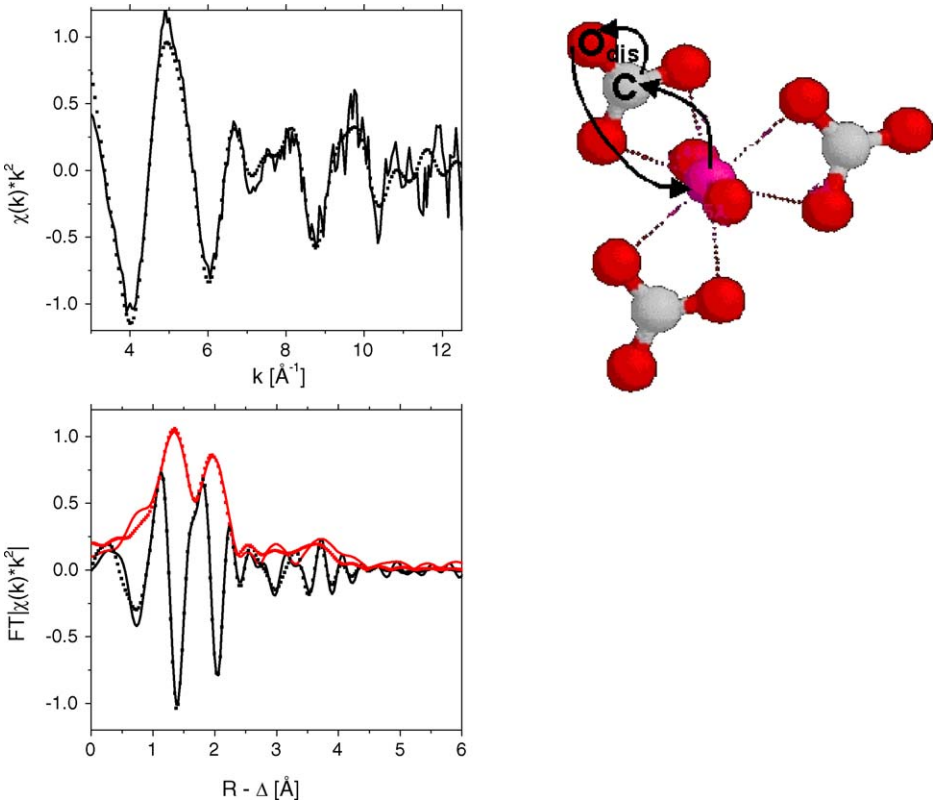

Fig. 7. U L3 EXAFS (top left) and corresponding Fourier transforms (bottom left) for an aqueous $UO_2(CO_3)_3^{4-}$ solution. Continuous lines are the experimental data; symbols represent a theoretical model of the data including MS (U → O*ax* → U → O*ax* → U and U → C → O*dis* → U) paths. (Top right) Model of the $UO_2(CO_3)_3^{4-}$ structure indicating the focusing effect leading to the increased amplitude of the O*dis* EXAFS. Data are taken from [51].

reported in [49]. Note in this case this does not lead to an increase in the EXAFS amplitude of the U–O*ax* FT peak. (MS peaks are never found in the FT spectrum at distances shorter than the second coordination shell.) Instead an additional FT peak is found at a distance about twice that of the U–O*ax* distance because, for this MS, R_{eff} is twice R(U–O*ax*).

We will discuss another example where MS is important for analysis of Cm L3 EXAFS for Cm(III) complexed with partitioning agents in Section 2.5.1.

2. Examples of actinide speciation using XAFS

The following examples presented in this section are not meant to be an exhaustive treatise on the theme of actinide speciation using XAFS in the field of nuclear waste disposal safety issues. Instead, I have selected examples which either illustrate important aspects of research dealing with nuclear waste disposal safety or of the XAFS method itself from my own recent research. Related work from other research groups are referenced as literature citations.

2.1. Characterization of eigencolloids

Essential for prediction of the amount of dissolved actinide species in a repository, which has been breached by water intrusion, is knowledge of the thermodynamic constants describing reaction equilibriums for released actinide cations. For example, solubility for the tetravalent actinides (An(IV)) is generally low at near-neutral pH values expected to be found in nature and therefore is a determinant factor in the immobilization of actinides released into the environment. The tetravalent actinides tend to form what are referred to as eigencolloids or polymerized hydrous oxyhydroxo polynuclear species at pH values moderately above the solubility of $An(OH)_4$(am). Reported literature solubility data, e.g., for Pu(IV), vary considerably. For this reason, new methods for determining the solubility constants using laser induced breakdown detection (LIBD) [60] have been developed [61]. By combining these LIBD investigations with Pu L3 EXAFS, the eigencolloids forming in solution have been characterized [62].

Investigation of the onset of Pu(IV) oxyhydroxide eigencolloid formation in an initially colloid-free Pu(IV) solution, detected by an increase in the LIBD signal as indication of exceeding the solubility limit (i.e., formation of colloids >5 nm in size), has been reported [62]. The points of colloid formation observed from LIBD (Fig. 8, circles and filled triangles) lie close to the lower limit of the $\log K^{\circ}_{sp} = -58.7 \pm 0.3$ reported in [63]. A linear dependency of log[Pu(IV)] on $-\log[H^+]$ with slope -2 is observed. Note that spectrophotometric investigations on a log[Pu(IV)] = -5 solution reveal a decrease in solvated Pu(IV) species below the solubility limit, without any observable increase in another Pu oxidation state. This decrease in signal is attributed to formation of small polynuclear oligomers formed by a fraction of the Pu(IV).

Independently, the structures of colloids formed upon increasing $-\log[H^+]$ was derived from their Pu L3 EXAFS spectra [62]. The spectra and FT data are shown in Fig. 9. Above

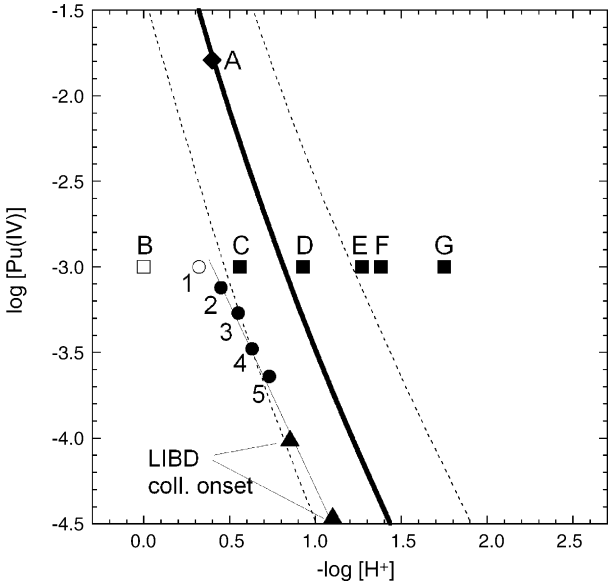

Fig. 8. Solubility curve of Pu(IV) using $\log K^{\circ}_{sp} = -58.7 \pm 0.3$ from [63]. Pu(IV) concentrations and $-\log[H^+]$ of EXAFS solution samples (squares and letters), colloid formation according to LIBD (circles and numbers) and colloid formation according to LIBD at Pu concentrations lower than 1 mM (triangles) are indicated.

the solubility limit the Pu–O shell splits, indicating formation of more than one bond length in this shell. The amplitude of the Pu–O shell increases with increasing $-\log[H^+]$. This indicates that colloids become more ordered as their size increases. The Pu–Pu distance at about R-Δ 3.6 Å is found in fits to the data to be nearly invariable of $-\log[H^+]$; it remains near that of $PuO_{2(cr)}$ (Fm3m; $a = 5.396$ Å) between 3.85 and 3.90 Å. The intensity of this Pu–Pu FT peak also increases with increasing $-\log[H^+]$. These observations are in agreement with formation of a –Pu–O–Pu– backbone with f.c.c. Pu sublattice in the colloids, which grows with increasing colloid size.

Combining the EXAFS and LIBD results, the authors offer a model for colloid formation. To be consistent with EXAFS, LIBD, and UV/vis data, monomeric solvated Pu(IV) species must begin to disappear before colloids >5 nm form, colloid formation must entail splitting of the nearest-neighbor oxygen shell, provide for the presence of a –Pu–O–Pu– backbone having f.c.c. Pu sublattice in the colloid structure, whose static order increases with colloid size, and involve a -2 slope dependency of solubility versus $-\log[H^+]$. A model for Pu(IV) eigencolloid formation consistent with these experimental results is via condensation of $Pu_nO_p(OH)_{4n-2p}(H_2O)_z$ oligomers, where the oligomers themselves form through condensation of $Pu(OH)_2(H_2O)_6^{2+}$ monomeric units (Fig. 10). The structure resulting from this proposed model has a –Pu–O–Pu– backbone with increasing structural order as the size of the colloids increases. The Pu–O coordination shell is expected to split due to the presence of different (O^{2-}, OH^-, and H_2O) ligands in the growing structural network. The highest degree of order is expected for the largest colloids with the highest degree of condensation, in accord with experimental results (sample G).

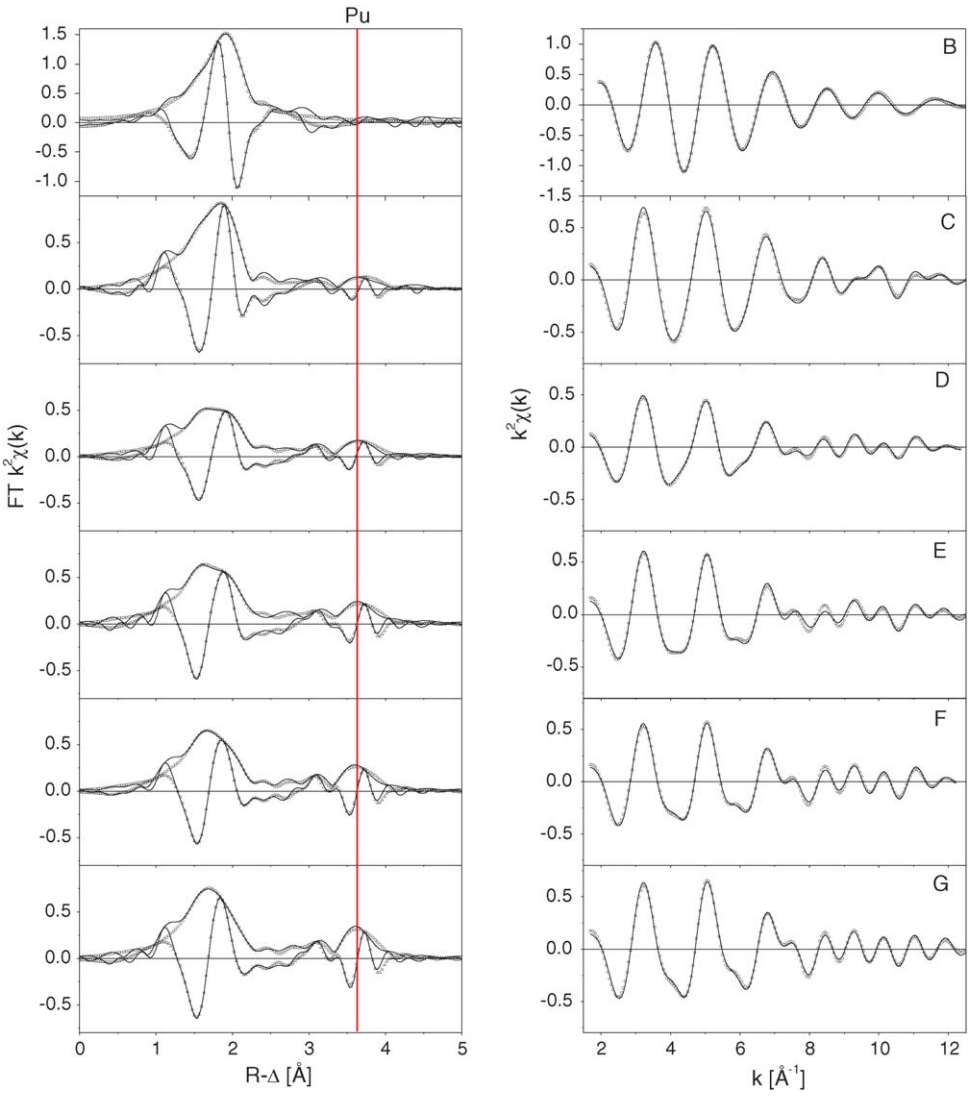

Fig. 9. (Left) FT magnitude of k^2-weighted EXAFS of the samples indicated in Fig. 8 data (solid line), FT imaginary part (thin solid line). (Right) Corresponding Fourier-filtered data. Open symbols corresponding fit curves for results reported in [62]. Dashed line marks Pu–Pu interaction. Note the different *y*-axis scale for sample B.

2.2. *Interaction of actinides with humic substances*

Much of the first work XAFS work on actinide elements complexed with naturally occurring organic polyelectrolytes, humic and fulvic acids (HA and FA, respectively) were reported in the 1990s [64–67]. Further, more recent reports are found in [68–71] XAFS investigations on these materials aim at understanding actinide-HA/FA interaction. The importance of such studies rests upon in the innate ability of HA and FA to complex metals, including the actinides, which renders them an important role in natural processes determining the mobility and fate of metal cations in the environment. HA and FA can potentially serve as vehicles for colloid mediated transport of actinides from a nuclear repository near-field to the far-field. HA and FA are naturally occurring water soluble organic substance with molecular mass distribution maxima around 500–600 g/mol [72]. HA/FA have numerous different functional groups, which are potential binding sites for metal cations. These include both hard and soft donor functional groups such as hydroxyl and carboxyl groups as hard donors; amino, sulfonyl, and thiol groups are examples of soft donor functional groups.

To illustrate the complexity and diversity of humic functional groups we examine S K edge XANES from HA reported in the literature [73–77]. Some of these reports are interesting, as they entail expert XAFS methodology often used, for example, spectromicroscopy for acquiring spatially resolved information [75,77] and principle component analysis (PCA) for determining proportions of multiple species which contribute to a measured spectrum [76].

An example of an S K edge spectrum of a commercially available HA (Aldrich) is shown in Fig. 11. The XANES has been fit with a arctan function to simulate the edge jump (held constant at 2.475 keV during the fit), a line to account for any incomplete background subtraction, and five Gauss functions, each representing contributions from various S containing functional groups (see Table 3). Assignments of the peaks is made

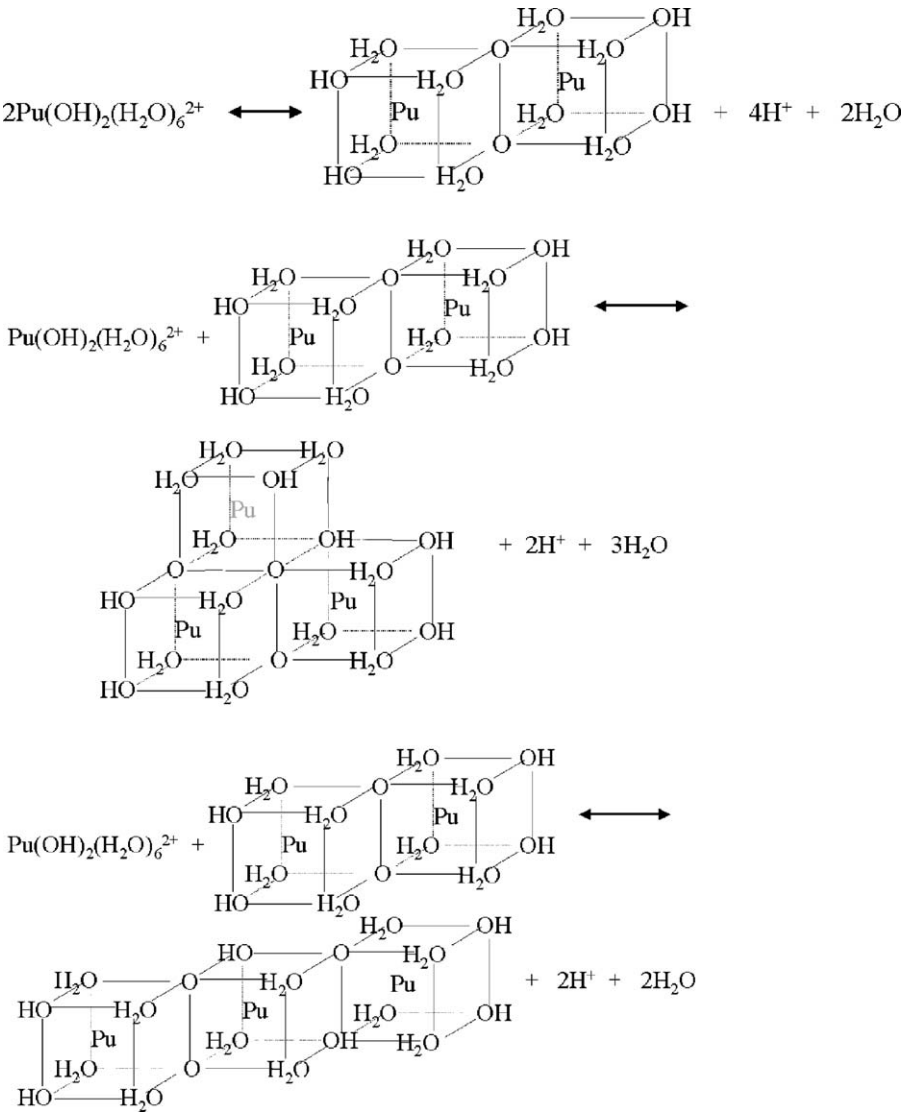

Fig. 10. Schematic representation of oligomer formation in Pu(IV) eigencolloid formation. (Top) Hydrolysis and condensation of two monomeric $Pu(OH)_2(H_2O)_6^{2+}$ units to an edge sharing, binuclear species. Formation of a trinuclear species through hydrolysis and condensation of a monomeric $Pu(OH)_2(H_2O)_6^{2+}$ unit with a binuclear species a double edge sharing species with a common corner (middle) or to form a single edge sharing species (bottom).

by comparison to the energy position of function groups in known compounds. Note that the intensities of these functional group peaks vary widely, depending on the source and history of the HA or FA. One can readily imagine the difficulties in research dealing with HA and FA, due to the complexity of these substances. Nevertheless, as XAFS is a method, which can be applied in situ, it has been successfully used to provide direct speciation of actinides in the presence of HA/FA under varying conditions. Since it is an element specific method, it allows the study of relatively 'dirty' or natural mixtures without prior separation.

Table 3
Energy position, peak assignment and peak areas for the Gauss curves from least squares fits to the S K XANES depicted in Fig. 11, see text for details

Energy position (keV)	Peak assignment	Peak area (a.u.)
2.4724	Disulfides (R–S–S–R′); polysulfides (R–S_n–R′)	209
2.4732	Monosulfides (R–S–R′); thiols (R–SH)	92
2.4749	Sulfonium (R–S^+–R′); sulfoxide (R–(S=O)–R′)	261
2.4799	Sulfone (R–SO_2–R′)	139
2.4813	Sulfate (SO_4^{2-}); ester sulfate (R–SO_3^-)	88

In the following, results of a study of the interaction of Np(IV) with FA are first discussed. This study demonstrates the type of coordination structure information available from EXAFS, which aids interpretation of observed complexation behavior of such a complex and heterogeneous system as FA. This is followed by a short discourse of recent results in the soft X-ray regime of using C 1s NEXAFS to fingerprint the interaction of HA with uranyl cations. In the hard X-ray regime, the U and Th L3 EXAFS studies from the 1990s mentioned above all indicate complexation to the metal cations via HA/FA carboxylate groups, with carboxylate groups bound to the metal cation in a monodentate fashion. By studying the C 1s transitions, efforts are made to obtain more detailed information of the metal–HA

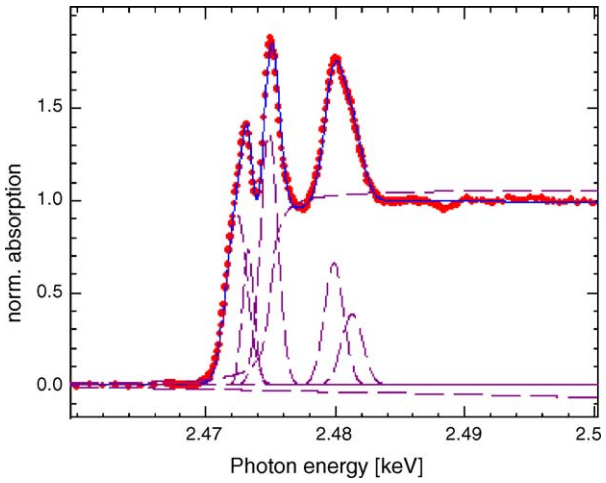

Fig. 11. S K edge XANES (dots) and least squares fit curve (continuous line) modeled using the individual functions shown (dashed lines) for an aqueous sample of purified Aldrich humic acid.

interaction from the perspective of the ligand, instead of from the metal cation in the L3 edge studies.

2.2.1. Np L3 EXAFS study of the interaction between Np(IV) and Gorleben fulvic acid

Tetravalent neptunium complexed with two different naturally occurring FA isolated from geological formations associated with proposed nuclear waste disposal sites, from Boom clay interstitial water in Belgium and Gorleben ground water in Germany, at H^+ concentrations of $10^{-1.0}$ and $10^{-1.5}$ M, has been investigated with EXAFS at the Np L3 edge (Fig. 12; [78]). The loading capacity (LC) of fulvates for Np(IV) exhibits an remarkably large increase going from pH 1.0 to 1.5 [79]. This study aimed at ascertaining if this anomalous LC increase is associated with a change in the metal–ligand interaction or the type of species formed.

Metrical parameters obtained from fits to the EXAFS oscillations using a model of two oxygen coordination shells are listed in Table 4. The Np(IV)-fulvate complex is observed to have two distinct nearest neighbor oxygen distances, 2.25 and 2.44 Å. From comparison to distances in known compounds, the shorter distance is interpreted as being attributed to a hydroxyl ligand; the longer one is an average Np–O distance for coordinating water molecules and carboxyl groups from the fulvate. No Np–Np scattering peak is observed in the EXAFS spectra. The Fourier-filtered oscillation of the Np–O FT peak for all samples (Fig. 13) shows a beat node interference pattern near $k \sim 9$ Å^{-1}. The presence of a beat node is evidence for the presence of two nearest neighbor oxygen distances. From the k value of the beat node (k_{bn}), the bond distance difference (ΔR) between the two interfering coordination shells is estimated [80] from $\Delta R = n(\pi/2k_{bn})$ to be 0.17 Å for these samples. This value is to within experimental error in accord with the fit results.

Table 4
Results of fits Fig. 12 and to the EXAFS data shown in described in the text

Sample	N	R (Å)	σ^2 (Å^2)	ΔE_0 (eV)
Np(IV):Gorleben-FA, $-\log[H^+] = 1.5$ (A)	3.4 5.8	2.25 2.43	0.001 0.003	−2.6
Np(IV):Gorleben-FA, $-\log[H^+] = 1.0$ (B)	3.7 7.1	2.26 2.43	0.001 0.005	−2.5
Np(IV):Boom clay-FA, $-\log[H^+] = 1.5$ (C)	4.2 5.0	2.27 2.44	0.005 0.005	−2.5
Np(IV):Boom clay-FA, $-\log[H^+] = 1.0$ (D)	2.3 6.6	2.24 2.41	0.001 0.006	−2.5
Np(IV) aquo ion (E)	10.5	2.39	0.005	−1.5

The EXAFS results show that the observed anomalous increase in LC of humic substances for Np(IV) with increasing pH is due to the presence of the mixed hydroxo-humate neptunium complex: $Np(OH)_xFA(IV\text{-}x)$, where FA(IV) denotes four functional groups from fulvate neutralizing the Np^{4+} cation charge. The presence of coordinating hydroxyl ligands, and not the formation of polynuclear species or a change in the metal–ligand interaction, leads to the unusually large calculated LC values.

2.2.2. STXM investigation of actinide complexation by humic acid

Scanning transmission X-ray microscopy (STXM) has proved to be a valuable tool for characterizing HA chemical

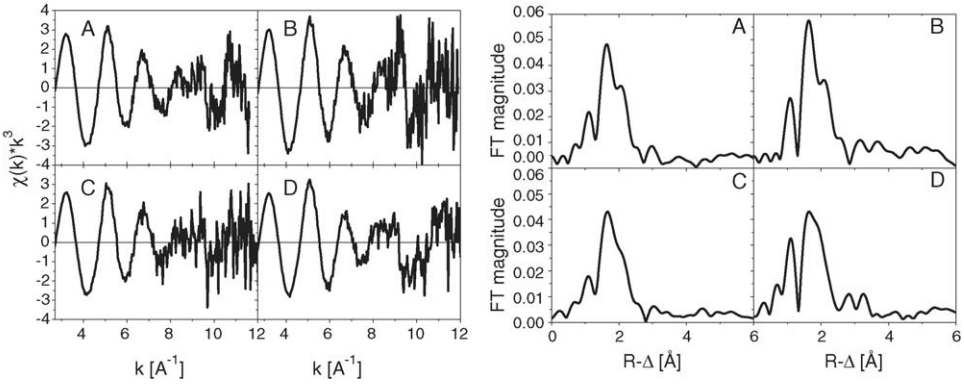

Fig. 12. k^3-weighted EXAFS (left) and their corresponding Fourier transforms (right) of the Np(IV)-fulvates studied. (A) Np(IV):Gorleben-FA, $-\log[H^+] = 1.5$; (B) Np(IV):Gorleben-FA, $-\log[H^+] = 1.0$; (C) Np(IV):Boom clay-FA, $-\log[H^+] = 1.5$; (D) Np(IV):Boom clay-FA, $-\log[H^+] = 1.0$.

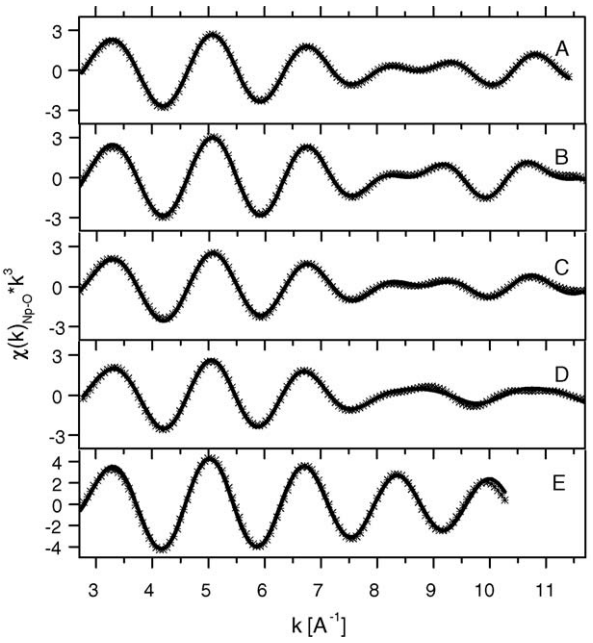

Fig. 13. Fourier-filtered first coordination shell EXAFS of the Np(IV)-fulvate spectra shown in Fig. 12 and of the Np(IV) aquo ion (E).

functionality with simultaneous visualization of HA morphology on a sub-μm scale [81–84]. By means of STXM both morphological and microchemical information can be obtained at the same time in situ on aqueous colloid species within the 'water window' (i.e., between the C 1s and O 1s absorption edges at 284 and 537 eV, respectively). Microscopic images of colloid morphology are obtained by raster-scanning selected sample areas using a beam spot in the nm range. C 1s NEXAFS provides direct speciation of carbon containing macromolecules from their characteristic 1s → π*, σ* resonances. C 1s NEXAFS spectra can be extracted from selected sample regions in stacks of microscopic images recorded a discrete energies [81]. One can also adjust the absorption contrast in images to differentiate carbonaceous from carbon-free material by recording images above and below the C 1s ionization energy or to highlight functional group distributions by recording images at NEXAFS peak energies assigned to the functional group of interest.

The normalized C 1s-NEXAFS spectra of purified Aldrich HA reacted with U(VI) are depicted in Fig. 14a and b. The spectrum of HA before metal loading is plotted in Fig. 14c. Similar to results in [85], the uncomplexed HA NEXAFS cannot be reproduced from a superposition of spectra extracted from image stacks of the complexes. This indicates that the spectral

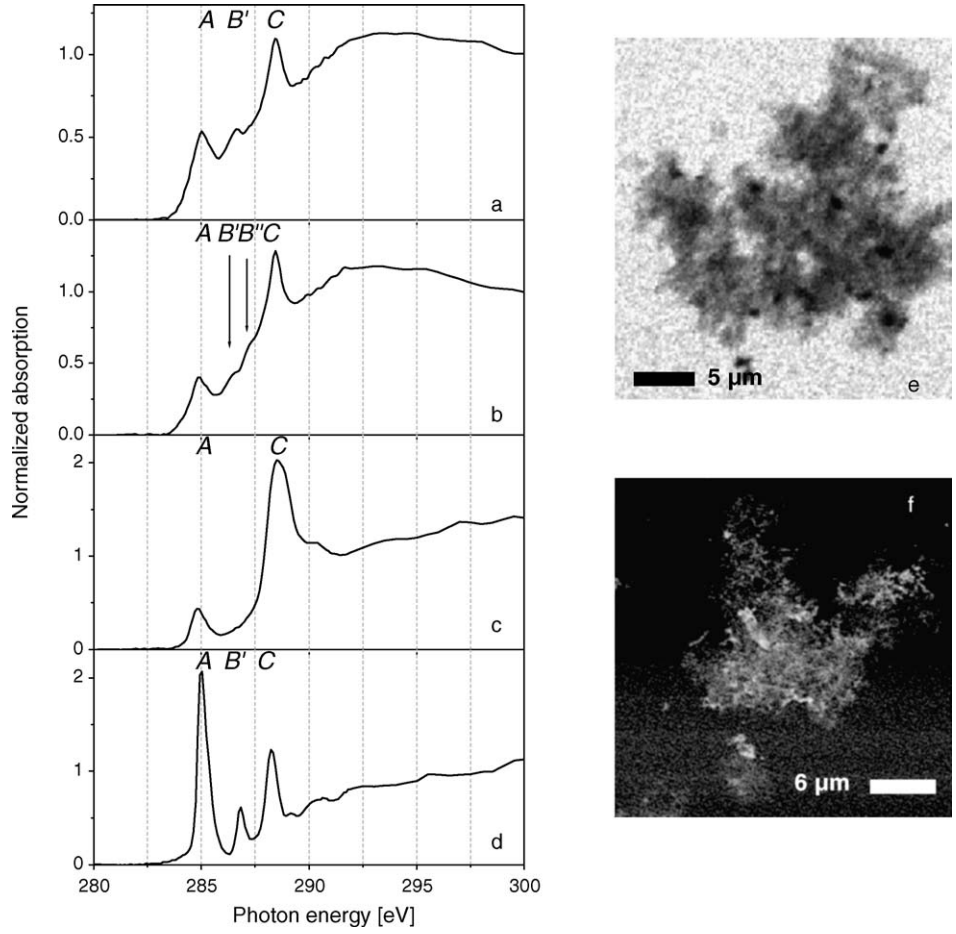

Fig. 14. C 1s NEXAFS of (a) U(VI)-HA (signature 1), (b) U(VI)-HA (signature 2, see text for details), (c) HA without metal loading, (d) 4-hydroxy benzoic acid, (e) STXM micrograph at 288.5 eV of U(VI)-HA aggregate and (f) STXM micrograph (contrast enhancing negative image) at 290 eV of HA aggregate at pH 4.3 (without metal loading).

changes observed upon metal complexation with HA result from distinct changes in the HA carbon molecular states. The STXM micrograph of a typical HA aggregate formed upon HA–metal interaction is depicted in Fig. 14e. The U(VI)-HA aggregates are similar to those formed for Eu(III)-HA, showing segregation of carbonaceous material into zones with different morphologies and optical densities [82]. Patches with higher optical density are found embedded in a less optical dense matrix. The STXM micrograph of unreacted HA (Fig. 14f) at pH 4.3, reveals a less dense, network-like structure with particles and larger sheets of carbonaceous material embedded in a fibrous network. At least two different C 1s-NEXAFS signatures characterize U(VI)-HA (Fig. 14a and b): a signature with a relatively strong phenolic resonance (C 1s (C_{ar} − OH) → $\pi^*_{C=C}$; position B′) and the second signature showing two shoulders B′ and B″. Peak positions and shapes can be assigned in accordance with model compound spectra such as substituted benzoic acids [86]. The energy of peak B′ (286.6 eV) coincides with the phenolic transition for 4-hydroxy benzoic acid (Fig. 14d) [87]. Transitions observed in the energy range near B′ are generally indicative of substituted aromatic carbon atoms, its intensity a measure of the number. The position of peak B′ correlates to the overall electronegativity of aromatic substituents [86]. This correlation is the basis for identification of the origin for this peak in U(VI)-HA and HA spectra as phenolic groups. However, the energy position of B′ is not observed to be affected by metal complexation. Resonance A represents the aromatic carbon (C_{ar}) in these compounds. Feature B″ is due to transitions from molecular states formed following metal complexation [82]. The intensity of the peak C in the HA spectrum, resulting from carboxyl C transitions (C 1s (COOH) → $\pi^*_{C=O}$), is observed to decrease upon complexation. The observed spectral changes and the similarity between the U(VI)-HA NEXAFS signatures and those for Eu(III)-HA reported in [87] are interpreted as evidence for a similar complexation mechanism, which involves HA carboxyl functional groups, for both metal cations. This corroborates the interpretation of hard X-ray U L3 EXAFS results [65,66].

2.3. Interaction of actinides with carbonate

The role of carbonate in natural actinide speciation has been the subject of much XAFS investigative work (for studies of Th-carbonates see [55,54], U-carbonate solution studies chemistry [88,52,53,56], Np-carbonate results [89,58] and Pu-carbonate investigations [90,57,59]). For a review of the role of carbonates in environmental actinide speciation see [91]. The reason for such studies lies in the fact that carbonate is an important complexing ligand and carbonate–bicarbonate equilibriums play a role in the pH of natural water systems. Carbonate minerals are involved in the steady-state balanced between the supply rate of carbonate to natural waters from weathering and the removal of carbonate by burial in sediments. The three major sedimentary carbonate minerals are calcite ($Ca(CO_3)_2$), aragonite, and dolomite ($CaMg(CO_3)_2$). Calcite is by far the most abundant carbonate mineral and comprises about 4 wt.% of the Earth's crust. Aragonite is less common, a polymorph of calcite, forms in, e.g., hot springs deposits, cavities in volcanic rocks, caves and mines, is found in shells of mollusks, in corals and pearls, and is metastable, eventually converting to calcite under most conditions.

Natural carbonate minerals can incorporate U(IV) and U(VI) into their structure, thereby forming solid solutions. In addition, a variety of stable uranyl carbonate minerals exist. In order to understand the potential of carbonate minerals for sequestering uranium (and other actinides), a number of XAFS studies of the structure of uranium incorporated into carbonate minerals have been reported [92–97]. Single calcite crystals formed from solutions of uranyl coprecipitated with calcite have been investigated with the aim of identifying whether incorporation occurs at structurally distinct surface sites [93]. μ-XRF results reveal significant differences in the distribution of uranium on non-equivalent vicinal faces of a growth hillock. The surface associated with – steps showed uranium-enrichment compared to the + surfaces. To corroborate these results, a grazing incidence (GI)-XAFS study of U(VI) cation sorption onto the natural cleavage plane of a calcite crystal has been reported. The results of this investigation are summarized in the following section.

2.3.1. Uranyl sorbed onto the (104) calcite surface

A polarization dependent EXAFS study of U(VI) cation sorption onto the natural cleavage plane of a calcite crystal in GI geometry has been reported [51]. The authors aimed at determining if there is a preferential sorption of uranyl cations onto steps on the calcite surface. Investigations by other groups report a differential incorporation of uranyl cations between the two symmetrically non-equivalent surfaces associated with growth at + and − steps during calcite single crystal growth [98]. The question arises if the step selective incorporation results from a site-selective sorption.

This investigation is one example of many reported in the literature using XAFS spectroscopy in the earth sciences for determining molecular structures of surface-sorbed species [99–112]. This particular example here has the added aspect that it demonstrates the use of GIXAFS as a surface sensitive tool for actinide speciation and utilizes the inherent linear polarization of synchrotron radiation to observe the polarization dependent XAFS signal as a function of sample orientation. The U(VI) cation is present in its stable form as linear $[O{=}U{=}O]^{2+}$ dioxouranium(VI) cation or 'uranyl' cation. Uranyl units oriented in a common direction exhibit distinct differences in their U L3 XAFS spectra, depending on their orientation relative to the polarization vector (ε) of the incident synchrotron beam [113,49].

By means of GI excitation [114] of metal cations sorbed onto a surface, the metal species sorbed at reactive surface sites can be characterized. For two examples of U(VI) sorption onto α-Al_2O_3 reported in the literature, see Refs. [115,116]. Investigations of monolayers and sub-monolayers of radionuclides on surface substrates are possible with this technique. A schematic representation of a GIXAFS set-up is shown in Fig. 15. Monochromatic synchrotron radiation (SR) is defined to a small horizontal width (<300 μm) by two horizontal slits. The sample chamber is on a high precision goniometer cradle, which allows high precision vertical and angular positioning.

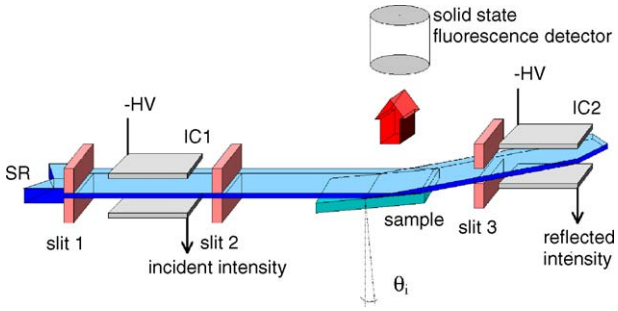

Fig. 15. Schematic representation of a grazing incidence XAFS (GIXAFS) experiment. SR: monochromatic synchrotron radiation; HV: high voltage; IC1 and IC2: first and second ionization chambers; θ_i: incident angle of the SR; bold arrow represents fluorescence radiation from the sample.

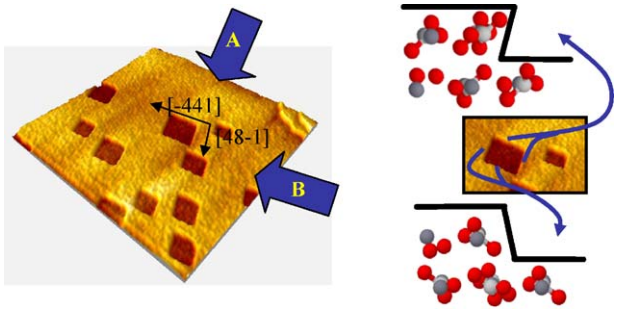

Fig. 17. (Left) In situ atomic force micrograph of a cleaved calcite (10–14) surface exposed to carbonate saturated aqueous solution (pH 8.3). Pits with molecular step edges parallel to [48-1] and [−441] are observed. The impinging beam during recording of the spectra designated A and B shown in Fig. 16 is indicated. Cartoon of the − steps (top right) and of the + steps (bottom right) and their location on the pits. The c-glide plane of the surface runs approximately diagonally across the pits.

The sample surface is oriented with respect to the impinging beam at an incident angle (θ_i) slightly below the critical angle for total external reflection. At such angles, the penetration depth into the sample surface is limited to a few nm. As in a standard XAFS experiment, the incident SR intensity is measured with an ionization chamber (IC1). The reflected beam is monitored with a second ionization chamber (IC2), placed horizontally higher than the IC1 at a position dependent on θ_i and the distance from the sample; the remaining fraction of transmitted beam is cut off at the lower jaw of a third horizontal slit. Fluorescent detection is also possible with a solid state detector placed at a right angle from the sample.

The k^2-weighted U L3 edge GIEXAFS and their corresponding FT spectra for a freshly cleaved natural calcite sample, previously treated with an alkaline carbonate aqueous solution containing uranyl cations are depicted in Fig. 16 [51]. Spectra were recorded using fluorescence detection at two different sample surface orientations relative to ε schematically indicated in Fig. 17. Because the calculated aqueous U speciation of the alkaline uranyl solution used to prepare the sorption sample is dominated by $UO_2(CO_3)_3^{4-}$, the EXAFS for the uranyl sorbed calcite is compared to that for a $UO_2(CO_3)_3^{4-}$ reference solution shown in Fig. 7. The MS 'triplet' oscillatory fingerprint between k 6.5 and 8.5 Å^{-1} observed in the $UO_2(CO_3)_3^{4-}$ EXAFS is missing in the EXAFS of the uranyl sorbed calcite in Fig. 16. From this, the authors concluded that the surface sorbed species was not simply the majority solution species, i.e., a tricarbonato species.

Qualitative examination of the two spectra in Fig. 16 shows that amplitude of the U–O*ax* shell in both spectra exhibit similar amplitudes, whereas the U–O*eq* signal in the **A** spectrum is significantly different than in the **B** spectrum. There are two possible explanations for this apparent non-variance in Θ(U–O*ax*) with ε. Either the linear $[O{=}U{=}O]^{2+}$ units are perpendicular to ε or they are oriented at a small constant 'tilt' relative to ε in both the A and B spectra. That Θ(U–O*eq*) is observed to change with relative orientation of ε to the crystal surface infers that the coordination of U(VI) in its equatorial plane is significantly asymmetric. Because at each orientation both + and − steps "see" the beam (compare cartoon in Fig. 17), a preferential sorption onto one of the steps likely occurs. Otherwise, both spectra A and B would be the same and they are not. Simple qualitative observation of the spectra allows to positively answer the question if a preferential sorption on one of the steps occurs. A more detailed analysis to identify which step is not given in [51], however.

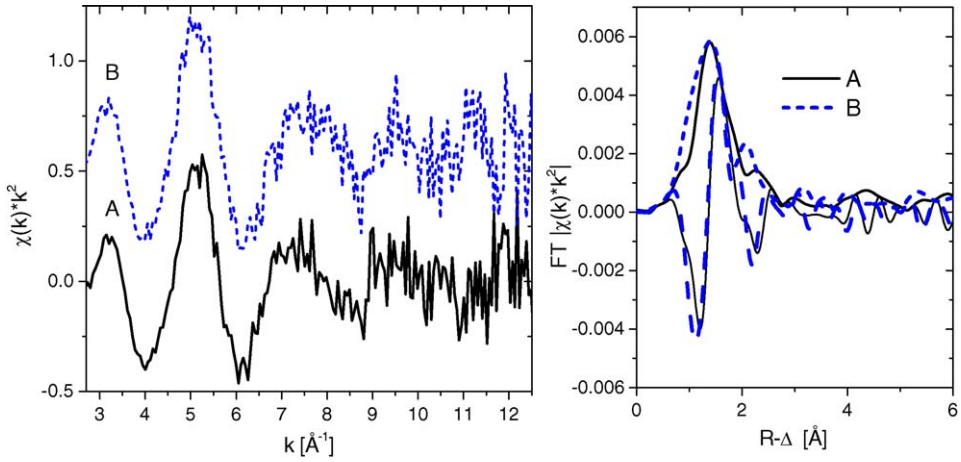

Fig. 16. U L3 GIEXAFS (left) and corresponding Fourier transforms (right) for the uranyl sorbed natural calcite (10–14) sample measured at two different angles relative to ε (ε is perpendicular to the arrows in Fig. 17).

2.4. A natural analogue XAFS study

Natural analogue sites for high level radioactive waste disposal repositories in deep geological formations are sites having geochemical and geological conditions which are similar to the overburden of host rocks for deep geological waste repositories [117]. Most, but not all (e.g., [118]), repository natural analogue sites have a natural uranium enrichment such as Alligator River Uranium Fields in the Northern Territory of Australia [119], Cigar Lake in Saskatchewan, Canada [120], Oklo-Okelobondo in the République Gabonaise [121], and the Ruprechtov site in the northwestern part of the Czech Republic [122]. The general aim of natural analogue investigations is to provide information on a long term scale, important for models used in repository performance assessment (PA). Of long term importance is evidence for the applicability of thermodynamic data and models extracted from laboratory experiments and field studies, based on short-term (and small-volume) scales, to PA of actual repositories over an exceedingly long time span (and large area/volumes).

Spatially resolved X-ray fluorescence (XRF) and XAFS investigations with a micrometer-scale resolution (μ-XRF and μ-XAFS) recorded in a confocal geometry on a bore core section from an clayey, lignite-rich uranium-enriched sediment from the Ruprechtov analogue site have been reported [123]. Previous reports of actinide speciation using spatially resolved XRF and XAFS investigations have appeared in the literature [43,124–126]. This study in confocal geometry, providing depth information, was the first of its kind. The authors' goal was to identify the uranium species in the sediment and determine if any preferential association of uranium with other elements occurs. The confocal irradiation-detection geometry [127,128] was employed during the experiments in order to define microvolumes, several tens to two hundred micrometers below the sample surface, from where fluorescent radiation was detected. By rastering sample areas at varying depth below the sample surface stacks of tomographic cross-sections of elemental distributions at varying depth were recorded (see Fig. 18). Framboidal Fe(II) nodules present in the sediment are seen as localized round-shaped areas of high Fe Kα fluorescence intensity in the Fe distribution map. A qualitative comparison of the Fe distribution with that for As reveals that these round-shaped Fe areas generally correspond to areas of low or no As Kα fluorescence intensity. Comparison of U distribution maps with those for distribution of As in As(V) and As(0) oxidation states in the same imaged areas (not shown; no evidence was found for As(III)) reveal U to be associated with As(V). As(0) is found to be intimately associated with the surface of Fe(II) nodules and comparison of its XANES to those of known compounds show it likely arsenopyrite.

U L3 μ-XANES spectra recorded at uranium-rich spots below the sample surface exhibit the XANES energy position as well as general shapes and intensities of the spectral features expected for U(IV) (Fig. 19). The characteristic XANES features for U(VI) (low WL intensity and MS feature 10–15 eV above the WL) are missing. The authors were also successful in recording the first confocal U L3 μ-EXAFS spectrum (Fig. 20). The FT

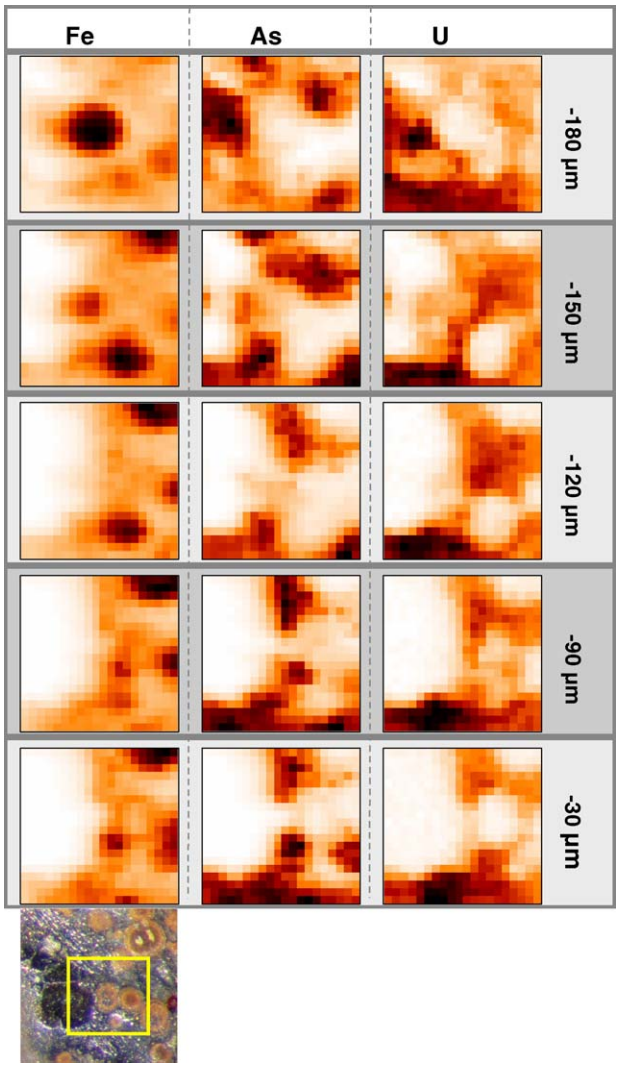

Fig. 18. Elemental distribution images for Fe, As, and U recorded at indicated depths below the surface (between −180 and −60 μm) of a 300 μm × 300 μm section of the Ruprechtov sediment sample studied marked in the optical photograph (left).

μ-EXAFS for the bore core shows no evidence of any short "yl" oxygen distance indicative of the presence of U(VI). The FT also exhibits two peaks, suggesting the presence of two coordination shells surrounding uranium. The bore core μ-EXAFS was well modeled with an O shell and a P shell. The coordination numbers and distances for both shells (8.1 O atoms at 2.33 Å and 6.2 P atoms at 3.65 Å) are comparable to that for the mineral ningyoite [129] and not uraninite [130]. The uranium species in the volume of the sediment investigated is a U(IV) phosphate mineral. The authors point out that, because the backscattering amplitude and phase shift functions for $Z+1$ atom types are so similar that they cannot be differentiated one from another, the U(IV) species may also be a sulfate.

Based on these results, the authors propose a mechanism of uranium immobilization in the Ruprechtov sediment, where arsenopyrite acted as reductant of ground water dissolved U(VI), originating from dissolution of uranium from nearby weathered granite, leading to precipitation of less soluble U(IV) and thereby

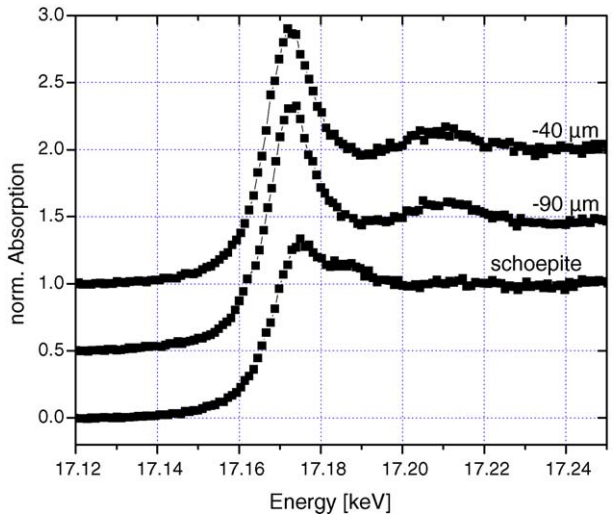

Fig. 19. U L3 μ-XANES recorded at −40 and −90 μm below the surface of an uranium-rich bore core section and compared to a solid U(VI) reference sample XANES (bottom).

forming As(V). The diagenesis processes leading to the formation of the phosphate is not yet clear.

2.5. Coordination structures of actinide/lanthanide cations complexed with partitioning ligands

The separation of trivalent actinides (An(III)) from lanthanides (Ln(III)) is a key step in the partitioning and transmutation (P and T) strategy [131], with the aim of separating long-lived radionuclides from spent nuclear fuels and transmuting them by nuclear fission into shorter-lived isotopes. This would have a positive impact on the long-term radiotoxicity of high-level nuclear wastes to be stored in a final geological repository.

Due to their chemical similarity, the task of An(III)–Ln(III) separation is a formidable one. Separation is not feasible using common oxygen-donor extractants; only complexation via soft donors such as sulfur or nitrogen atoms yields the desired selectivity [132]. To understand this selectivity, as well as to optimize partitioning extractant properties, much interest is devoted to finding a relationship between structural or electronic properties of partitioning ligand complexes of An(III) and Ln(III) cations and selectivity or extraction performance. To this end, a number of investigation of An(III)/Ln(III) complexed with candidate partitioning ligands have been reported in the literature [133–135]. A summary of one such studies is presented in the following. It is a comparative EXAFS study of Cm(III) and Eu(III) complexed with 2,6-di(5,6-dipropyl-1,2,4-triazin-3-yl)pyridine ($(n\text{-}C_3H_7)_4$-BTP). What the reader should note is in this study, is that it belongs to a momentary noticeable trend in the EXAFS community of combining EXAFS analysis with theoretical, either quantum chemical or molecular dynamic, calculations (see, e.g., [136–139]). In this particular example, EXAFS is combined with another spectroscopic technique, time-resolved laser fluorescence spectroscopy (TRLFS), and with quantum chemical calculations.

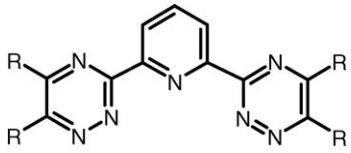

Fig. 21. Alkylated 2,6-di(1,2,4-triazin-3-yl)pyridines. R = CH_3, C_2H_5, n-C_3H_7, i-C_3H_7, n-C_4H_9, i-C_4H_9. In this study, R = n-C_3H_7.

2.5.1. Cm(III) and Eu(III) complexed with $(n\text{-}C_3H_7)_4$-BTP

Alkylated 2,6-di(1,2,4-triazin-3-yl)pyridines (BTPs, Fig. 21) are highly effective extractants for the separation of minor An(III) (americium, curium) from Ln(III) [140,141] in aqueous solutions of rather high acidity, up to 1 M nitric acid. The coordination structure of $(n\text{-}C_3H_7)_4$-BTP complexes of Cm(III) and Eu(III) using EXAFS analysis has been reported [142]. The measured Cm and Eu L3 edge EXAFS spectra and theoretical fit curves are shown in Fig. 22. Initial fits to the data using a model of two coordination shells revealed that the number of coordinating N atoms in the first shell is ∼9 and twice as many C/N atoms comprise the second shell. This indicates three ligands are bound to both Cm(III) and Eu(III). Note that because C and N are $Z+1$ elements, EXAFS cannot differentiate between them as backscattering nearest neighbors. The data was modeled with four coordination shells: nine nearest N atoms directly bound to the metal cations, second and

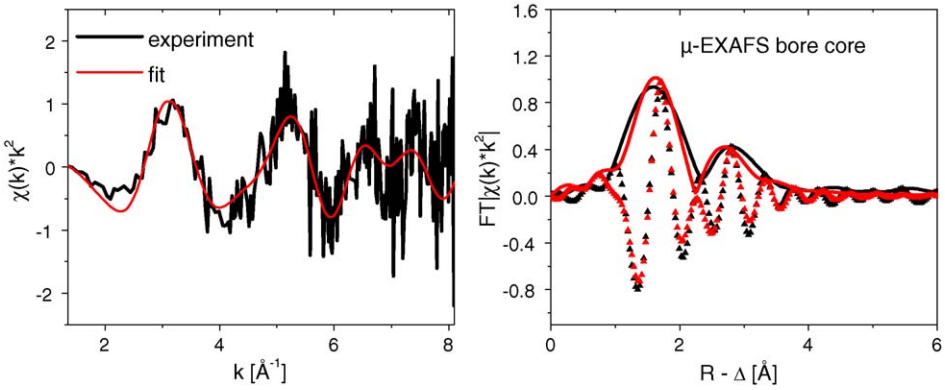

Fig. 20. U L3 μ-EXAFS (left) from an uranium-rich volume in the bore core and corresponding Fourier transformed data (right; magnitude in solid lines and imaginary part as symbols). Experimental data are shown in black and the fit result in grey.

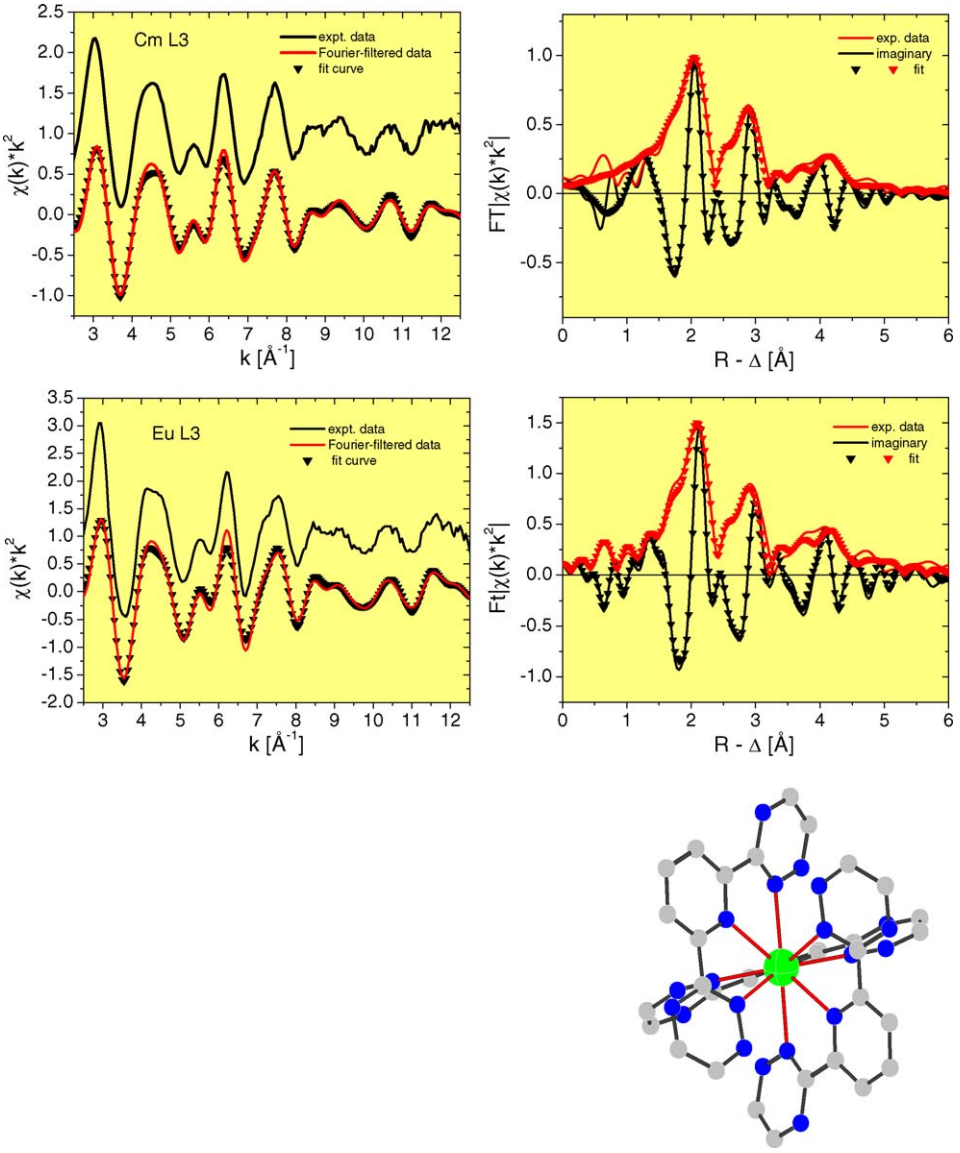

Fig. 22. Cm and Eu L3 k^3-weighted EXAFS for the extracted (n-C_3H_7)$_4$-BTP complexes together with their corresponding Fourier-filtered data and back-transformed fit (top left) and FT EXAFS magnitude, FT imaginary part together with corresponding R-space fit results (top right). Right: Structure of the Cm/Eu-[(n-C_3H_7)$_4$-BTP]$_3$ complex (H atoms and n-propyl groups not shown).

third shells of 18 C/N atoms each (designated C/N and C′/N′, respectively), and a fourth, most distant shell of nine C atoms corresponding to the C atoms para to the ligating N atoms in the heterocyclic rings (see Fig. 21). Three significant three-legged multiple scattering paths (Cm/Eu → N → C/N → Cm/Eu, Cm/Eu → C/N → C′N′ → Cm/Eu, and Cm/Eu → N → C′/N′ → Cm/Eu paths) were included in the fits with their effective path lengths correlated to single scattering distances involved and Debye–Waller factors varied. The n-propyl groups of the triazin rings were not included. The results are listed in Table 5. Note that the angles of the MS included in the fits are not exactly 180° and one might not expect them to make a large focusing effect contribution (compare Section 1.2.6). However, the sheer number of paths involved (e.g., all but one of the MS paths have a degeneracy of 36 each) renders their contribution significant.

Note the authors did not use a model to fit the first coordination shell using O atoms. Because EXAFS cannot differentiate between $Z+1$ elements, it also cannot differentiate between O and N atoms. However, in this system any coordinating O atoms would be from ligating nitrate groups and no evidence for coordinated nitrate groups in FTs of the fit residuals of back-transformed spectra is observed. Bidentate coordinated nitrate groups should show a nitrate N atom near 3 Å. This distance does not coincide with any C/N distances found in the complexes (Table 5) so that coordinated nitrate (formally required for charge neutralization) can be excluded.

Comparison of results in Table 5 shows that those for Cm are not significantly different than those for Eu, indicating that the coordination structure of Cm-[(n-C_3H_7)$_4$-BTP]$_3$ and Eu-[(n-C_3H_7)$_4$-BTP]$_3$ are the same. The observed selectivity of (n-C_3H_7)$_4$-BTP for Cm(III) over Eu(III) is not structural in origin;

Table 5
Metric parameters from fits of Cm/Eu L3 edge R-space data in Fig. 22 and compared to the Ce near structure in Ce[$(CH_3)_4$-BTP]$_3$

Sample	Shell	N[a]	R (Å)	σ^2 (Å^2)	ΔE_0 (eV)	r-factor[b]
Cm-[$(n$-$C_3H_7)_4$-BTP]$_3$	N	9	2.568 (0.007)	0.0051 (0.0007)	1.1 (0.8)	0.025
	C/N	18	3.431 (0.009)	0.005 (0.001)		
	C/N	18	4.81 (0.03)	0.004 (0.003)		
	C	9	5.30 (0.04)	0.001 (0.006)		
Eu-[$(n$-$C_3H_7)_4$-BTP]$_3$	N	9	2.559 (0.008)	0.0044 (0.0008)	2.5 (0.9)	0.028
	C/N	18	3.42 (0.01)	0.006 (0.001)		
	C/N	18	4.82 (0.02)	0.004 (0.003)		
	C	9	5.30 (0.03)	−0.002 (0.003)		
Ce[$(CH_3)_4$-BTP]$_3$[c]	N	9	2.618			
	C/N	18	3.485			
	C/N	18	4.770			
	C	9	5.282			

Estimated standard deviations are listed in parentheses and do not include systematic errors. S_0^2 is fixed at 1.
[a] Held constant at given values.
[b] Parameter describing goodness of fit = weighted sum of squares of residuals divided by the degree of freedom.
[c] From [147].

the metal cation complexes coordinated with three ligands have the same coordination structure.

The Cm L3 EXAFS data was also analyzed using a newly reported method of Monte Carlo simulation [143]. The Monte Carlo (MC) simulation allows to model the three-dimensional structure of the complexes by using the experimental XAS spectra and the structure of the interacting ligand as constraints. In the MC simulation, the Cm atom was randomly moved in a sphere relative to one BTP molecule and the scattering contributions of the ligand atoms were multiplied by a factor 3. The center of the sphere, with a diameter of 10 Å, was located at the pyridine N atom. For around 1 million random positions of Cm in the sphere, the corresponding theoretical EXAFS spectra were compared with the experimental EXAFS spectrum. The average first shell Cm–N bond distance determined by the MC approach is 2.57 Å, which is

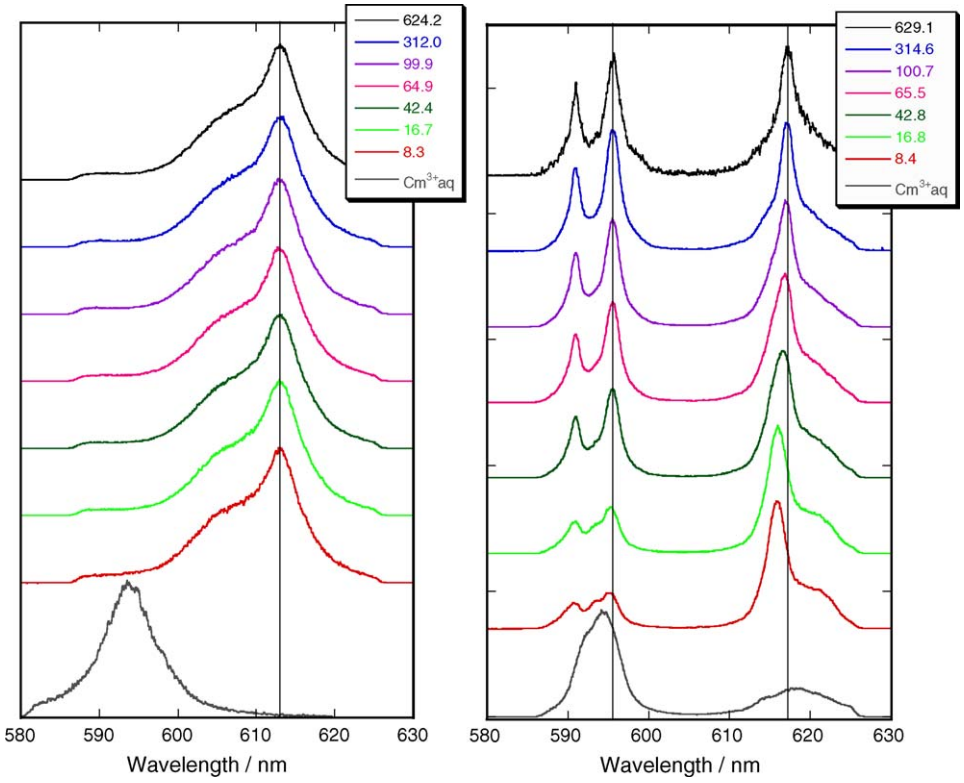

Fig. 23. Fluorescence spectra of Cm(III) (left) and Eu(III) (right) as a function of ligand-to-metal concentration ratio indicated in the legend (inverted series) compared to that for the Cm^{3+} and Eu^{3+} aquo species (bottom).

in excellent agreement with the conventional shell fit result (Table 5).

Density functional theory (DFT) calculations, unrestricted in the case of Cm(III), were carried out with several functionals available in TURBOMOLE V5.7 software package [144]. In all cases, metal-N distances and the differences between Cm-[(n-C_3H_7)$_4$-BTP]$_3$ and Eu-[(n-C_3H_7)$_4$-BTP]$_3$ are <0.01 Å, in agreement with experiments, The authors concluded that DFT gives the same metal–ligand bond distances to BTP for these two ions within the error bars. Additional optimization for Eu-[(n-C_3H_7)$_4$-BTP]$_3$ at the RI-MP2 level correlating the 5s, 5p shells on Eu(III) and all electrons of the ligand except the 1s electrons of C and N gave an averaged Eu–N bond distance of 2.554 Å, which is in excellent agreement with the EXAFS data.

TRLFS fluorescence spectra for Cm(III) and Eu(III) complexation with varying (n-C_3H_7)$_4$-BTP ligand to metal concentration ratios ([L]/[M]) are depicted in Fig. 23 and compared to that for the Cm^{3+} and Eu^{3+} aquo species. The Cm fluorescence is invariant of [L]/[M]; Cm(III) is observed to form only one species, Cm-[(n-C_3H_7)$_4$-BTP]$_3$. The formation of 1:1 or 1:2 complexes is not observed for [L]/[M] > 8.

In contrast, Eu(III) forms at least two different species for the varying [L]/[M] studied. Comparison with the literature shows that the fluorescence spectrum at high [L]/[M] (>300) is identical to the Eu-[(i-C_3H_7)$_4$-BTP]$_3$ measured in water/ethanol [145], meaning that at [L]/[M] > 300 the 1:3 complex is formed. Cm-[(n-C_3H_7)$_4$-BTP]$_3$ forms at much lower [L]/[M] than Eu-[(n-C_3H_7)$_4$-BTP]$_3$. This demonstrates that the higher affinity (corresponding to a larger formation constant) of (n-C_3H_7)$_4$-BTP toward An(III) cations over Ln(III) cations is the basis for the observed selectivity of BTP ligands in liquid/liquid extraction. Combining structural and spectroscopic results allowed understanding the ligand selectivity for Cm(III) over Eu(III). It is associated with a higher affinity and not associated to simple structural differences between complexes, as EXAFS and quantum chemical results show there is no difference between coordination structure of Cm-[(n-C_3H_7)$_4$-BTP]$_3$ and Eu-[(n-C_3H_7)$_4$-BTP]$_3$.

3. Conclusions and outlook

As a conclusion let us reiterate the information content of this review. The examples of actinide speciation using XAFS presented cover a broad range of topics in actinide science dealing with nuclear waste disposal. Examples of basic research topics in this field including aqueous actinide chemistry, colloid mediated transport of actinides, immobilization or retardation of actinide transport via sorption onto mineral surfaces, as well as coordination chemistry in non-aqueous solvents for partitioning research with the long term aim of reducing radiotoxicity of nuclear repository inventory have been described. Embedded within these examples are some basic as well as advanced aspects of the XAFS technique. The reader should be familiar with the type of electronic structure information in the C 1s near edge region, with determining valence from XANES spectra, with photoelectron multiple scattering in the EXAFS regime and the special case of focusing effect for collinear atoms, with surface sensitive grazing incidence measurements, with the fact that synchrotron light is linearly polarized and its utility for characterizing anisotropic systems, as well as with the option of having spatial resolution in experiments using nano- and micro-focused X-ray beams and the added advantage of obtaining depth information using confocal geometry.

A number of strategies for EXAFS data evaluation are also presented ranging from simple qualitative observation, to analysis of beat-nodes in the EXAFS interference pattern of two interatomic distances, up to newer approaches in XAFS data analysis such as Monte Carlo methods. It is good practice to always perform a qualitative analysis of the data prior to any fit procedure. If there is a discrepancy between numerical, metrical results of the subsequent fit with what the original qualitative analysis predicts, then one must critically question if the fit result actually has yielded the correct structural model. As in any data modeling procedure, it is important to check the correlation between fit parameters, calculate or estimate (for unknown noise levels) errors, and verify that a true minimum has actually been reached. A word of caution here is to emphasis the importance of not exceeding the number of independent parameters one is statistically allowed to vary in a multi-parameter, model-dependent fit of EXAFS data. The number of parameters one may vary depends on the available data. For fits of bond distances in the 1.7–4 Å range, using a $\chi(k)$ data set covering 2.5–15 $Å^{-1}$, the number of free variables (N_{free}) is about 18 ($N_{free} = 2\,\Delta R\,\Delta k/\pi$). The EXAFS equation (Eq. (6)) is generally modeled using up to four parameters for each shell (N, R, σ^2, and ΔE_0, the relative shift in E_0), the other parameters are used from references or theoretical calculations. This would allow for N_{free} of about 18 parameters modeling of up to four shells, four parameters each, at best.

In this review I have also attempted to demonstrate the strength of combining XAFS with other spectroscopies, analytical methods, and theoretical calculations. Examples in this review specifically being LIBD, spectrophotometry, microscopic techniques, and TRLFS. Combination with other spectroscopies and techniques often leads to corroboration of results but can also be used for refining the modeling of data or identification of systems with actinide cations in a number of different environments. It is highly advantageous to input any auxiliary information from other techniques into models used for multi-parameter fits to EXAFS data or for deconvolution of spectra. XAFS spectroscopy yields information averaged over the entire system, i.e., an average valence or average structure of a sample is obtained as a result. One must be sure that the actinide of interest in the system investigated is not present in an adventitious form or present in multiple environments. If such is the case and the data are evaluated as a single species, incorrect speciation information (structure, valence, functional groups) will be obtained.

As a final word of caution in conclusion I would like to point out the challenges facing experimentalists in studies of actinide speciation in repository far-field scenarios. Such scenarios necessarily deal with dilute systems in a heterogeneous environment. In these cases, it is difficult to obtain data with good signal-to-noise levels. As a result, the high noise at large k

in *k*-weighted EXAFS spectra leads to a limited useable *k*-range. To further complicate matters, the actinide of interest is often present as a mixture of species in a heterogeneous environment. Because of both of these effects, one can often only obtain information concerning the first coordination sphere in such systems. This limits possible interpretation of the data. Let us consider the example of the U(IV) phosphate mineral identification from the U L3 μ-EXAFS presented in Section 2.4 to explore this point. If the data quality from the bore core volume investigated were not sufficient to observe the second coordination shell, than no identification of the mineral would be possible. Knowing the U–O distance alone would be insufficient criteria to differentiate between UO_2 and a U(IV) phosphate; the interpretation rests on information from the second coordination shell.

References

[1] Proceedings of the OECD-NEA Workshop on Speciation Techniques and Facilities for Radioactive Materials at Synchrotron Light Sources, Grenoble, France, October 4–6, 1998.
[2] Proceedings of the Second OECD-NEA Workshop on Speciation Techniques and Facilities for Radioactive Materials at Synchrotron Light Sources, Grenoble, France, September 10–12, 2000.
[3] Proceedings of the Third Workshop on Speciation, Techniques and Facilities for Radioactive Materials at Synchrotron Light Sources, Berkeley, CA, USA, September 14–16, 2004.
[4] Proceedings of the Fourth Workshop on Speciation, Techniques and Facilities for Radioactive Materials at Synchrotron Light Sources, Karlsruhe, Germany, September 18–20, 2006.
[5] D.C. Koningsberger, R. Prins (Eds.), X-ray Absorption: Principles, Applications, Techniques of EXAFS, SEXAFS, and XANES, Wiley, New York, 1988.
[6] P.A. Lee, P.H. Citrin, P. Eisenberger, B.M. Kincaid, Rev. Mod. Phys. 53 (1981) 769.
[7] J.E. Penner-Hahn, Coord. Chem. Rev. 249 (2005) 161.
[8] B.K. Teo, EXAFS: Basic Principles and Data Analysis, Springer-Verlag, Berlin, 1985.
[9] Projected to be complete within the next five years.
[10] W. Matz, N. Schell, G. Bernhard, F. Prokert, T. Reich, J. Claußner, W. Oehme, R. Schlenk, S. Dienel, H. Funke, F. Eichhorn, M. Betzl, D. Pröhl, U. Strauch, G. Hüttig, H. Krug, W. Neumann, V. Brendler, P. Reichel, M.A. Denecke, H. Nitsche, J. Synchrotron. Rad. 6 (1999) 1076.
[11] H. Shiwaku, T. Yaita, Y. Okamoto, S. Suzuki, T. Harami, S. Inoue, T. Kudo, T. Tanida, Proceedings of the Third Workshop on Speciation, Techniques, and Facilities for Radioactive Materials at Synchrotron Light Sources, Berkeley, CA, USA, 2004.
[12] D. Grolimund, A.M. Scheidegger, J.F. van der Veen, R. Abela, PSI Sci. Rep. 4 (2002) 139.
[13] M.A. Denecke, J. Rothe, K. Dardenne, H. Blank, J. Hormes, Physica Scripta T115 (2005) 1001.
[14] H. Winick, Sci. Am. (1987) 72.
[15] J.C. Fuggle, N. Mårtensson, J. Elect. Spec. 21 (1980) 275.
[16] L.G. Parratt, C.F. Hempstead, E.L. Jossem, Phys. Rev. 105 (1957) 1228.
[17] http://physics.nist.gov/PhysRefData/Xcom/Text/XCOM.html.
[18] E.S. Marcos, M. Gil, J.M. Martinez, A.M. Munoz-Paéz, A.S. Marcos, Rev. Sci. Instrum. 65 (1994) 2153.
[19] U. Neuhäusler, S. Abend, C. Jacobsen, G. Lagaly, Colloid Polym. Sci. 277 (1999) 719.
[20] http://chemistry.anl.gov/heavy-element/actinide/multiple.html.
[21] L. Tröger, D. Arvanitis, K. Baberschke, H. Michaelis, U. Grimm, E. Zschech, Phys. Rev. B 46 (1992) 3283.
[22] J. Goulon, C. Goulon-Ginet, R. Cortes, J.M. Dubois, J. Phys. 43 (1982) 539.
[23] J.M. Traquada, R. Ingalls, Phys. Rev. B28 (1983) 3520.
[24] P. Eisenberger, G.S. Brown, Solid State Commun. 29 (1979) 481.
[25] J.M. deLeon, J.J. Rehr, S.I. Zabinsky, R.C. Albers, Phys. Rev. B44 (1991) 4146.
[26] A.L. Ankudinov, S.D. Conradson, J.M. deLeon, J.J. Rehr, Phys. Rev. B 57 (1998) 7518.
[27] J.J. Rehr, R.C. Albers, Rev. Mod. Phys. 72 (2000) 621.
[28] E.A. Stern, M. Newville, B. Ravel, Y. Yacoby, D. Haskel, Physica B 208/209 (1995) 117.
[29] M. Newville, J. Synch. Rad. 8 (2001) 322.
[30] N. Binsted, EXAFS analysis program EXCURVE, 1982.
[31] S.J. Gurman, N. Binsted, I.J. Ross, J. Phys. C 17 (1984) 143.
[32] A. Filipponi, A.D. Cicco, T.A. Tyson, C.R. Natoli, Solid State Commun. 78 (1991) 265.
[33] A. DiCicco, Physica B 208/209 (1995) 125.
[34] A. DiCicco, J. Phys. IV Colloque C2 (1997) 171.
[35] T. Ressler, J. Phys. IV 7-C2 (1997) 269.
[36] G.N. George, I.J. Pickering, EXAFSPAK: A Suite of Computer Programs for Analysis of X-ray Absorption Spectra, Stanford Synchrotron Radiation Laboratory, Stanford, CA, USA, 1993.
[37] A. Michalowicz, EXAFS pour le Mac, Logiciels pour la Chimie, Societé Francaise de Chimie, 1991, p. 102.
[38] P.M. Bertsch, D.B. Hunter, S.R. Sutton, S. Bajt, M.L. Rivers, Environ. Sci. Technol. 28 (1994) 980.
[39] M.A. Denecke, K. Dardenne, C.M. Marquardt, Talanta 65 (2005) 1008.
[40] S.D. Conradson, I. AlMahamid, D.L. Clark, N.J. Hess, E.A. Hudson, M.P. Neu, C.E. Palmer, W.H. Runde, C.D. Tait, Polyhedron 17 (1998) 599.
[41] O.C. Lind, B. Salbu, K. Janssens, K. Proost, H. Dahlgaard, J. Environ. Rad. 81 (2005) 21.
[42] P.J. Panak, C.H. Boothe, D.L. Caudler, J.J. Bucher, D.K. Shuh, H. Nitsche, Radiochim. Acta 90 (2002) 315.
[43] M.C. Duff, D.B. Hunter, I.R. Triay, P.M. Bertsch, D.T. Reed, S.R. Sutton, G. Shea-McCarthy, J. Kitten, P. Eng, S.J. Chipera, D.T. Vaniman, Environ. Sci. Technol. 33 (1999) 2163.
[44] M.R. Antonio, C.W. Williams, L. Soderholm, Radiochim. Acta 90 (2002) 851.
[45] J. Rothe, M.A. Denecke, V. Neck, R. Mueller, J.I. Kim, Inorg. Chem. 41 (2002) 249.
[46] J. Rothe, C. Walther, M.A. Denecke, T. Fanghänel, Inorg. Chem. 43 (2004) 4708.
[47] G.R. Choppin, A.H. Bond, P.M. Hromadka, J. Radioanal. Nucl. Chem. 219 (1997) 203.
[48] C. DenAuwer, E. Simoni, S. Conradson, C. Madic, Eur. J. Inorg. Chem. (2003) 3843.
[49] E.A. Hudson, P.G. Allen, L.J. Terminello, M.A. Denecke, T. Reich, Phys. Rev. B 54 (1996) 156.
[50] M.A. Denecke, Proceedings of the OECD-NEA Workshop on Speciation, Techniques and Facilities for Radioactive Materials at Synchrotron Light Sources, NEA, Grenoble, France, 1998, p. 135.
[51] M.A. Denecke, D. Bosbach, K. Dardenne, P. Lindqvist-Reis, J. Rothe, R.Z. Yin, Physica Scripta T115 (2005) 877.
[52] T.I. Docrat, J.F.W. Mosselmans, J.M. Charnock, M.W. Whiteley, D. Collison, F.R. Livens, C. Jones, M.J. Edmiston, Inorg. Chem. 38 (1999) 1879.
[53] G. Bernhard, G. Geipel, V. Brendler, H. Nitsche, Radiochim. Acta 74 (1996) 87.
[54] N.J. Hess, A.R. Felmy, D. Rai, S.D. Conradson, Mater. Res. Soc. Symp. Proc. 465 (1997) 729.
[55] A.R. Felmy, D. Rai, S.M. Sterner, N.J. Mason, N.J. Hess, J. Sol. Chem. 26 (1997) 233.
[56] D. Rai, N.J. Hess, A.R. Felmy, D.A. Moore, M. Yui, Radiochim. Acta 82 (1998) 17.
[57] D. Rai, N.J. Hess, A.R. Felmy, D.A. Moore, M. Yui, Radiochim. Acta 84 (1999) 159.
[58] D. Rai, N.J. Hess, A.R. Felmy, D.A. Moore, M. Yui, P. Vitorge, Radiochim. Acta 84 (1999) 89.

[59] D.L. Clark, S.D. Conradson, D.W. Keogh, P.D. Palmer, B.L. Scott, C.D. Tait, Inorg. Chem. 37 (1998) 2893.
[60] F.J. Scherbaum, R. Knopp, J.I. Kim, Appl. Phys. B 63 (1996) 299.
[61] V. Neck, J.I. Kim, B.S. Seidel, C.M. Marquardt, K. Dardenne, M.P. Jensen, W. Hauser, Radiochim. Acta 89 (2001) 439.
[62] J. Rothe, C. Walther, M.A. Denecke, T. Fanghänel, Inorg. Chem. 43 (2004) 4708.
[63] R. Knopp, V. Neck, J.I. Kim, Radiochim. Acta 86 (1999) 101.
[64] M.A. Denecke, D. Bublitz, J.I. Kim, H. Moll, I. Farkes, J. Synchrotron. Rad. 6 (1999) 394.
[65] M.A. Denecke, T. Reich, S. Pompe, M. Bubner, K.-H. Heise, H. Nitsche, P.G. Allen, J.J. Bucher, N.M. Edelstein, D.K. Shuh, K.R. Czerwinski, Radiochim. Acta 82 (1988) 103.
[66] M.A. Denecke, S. Pompe, T. Reich, H. Moll, M. Bubner, K.H. Heise, R. Nicolai, H. Nitsche, Radiochim. Acta 79 (1997) 151.
[67] S. Pompe, M. Bubner, M.A. Denecke, T. Reich, A. Brachmann, G. Geipel, R. Nicolai, K.-H. Heise, H. Nitsche, Radiochim. Acta 74 (1996) 135.
[68] K. Schmeide, T. Reich, S. Sachs, V. Brendler, K.-H. Heise, G. Bernhard, Radiochim. Acta 93 (2005) 187.
[69] S. Sachs, K. Schmeide, T. Reich, V. Brendler, K.-H. Heise, G. Bernhard, Radiochim. Acta 93 (2005) 17.
[70] K. Schmeide, S. Sachs, M. Bubner, T. Reich, K.-H. Heise, G. Bernhard, Inorgan. Chim. Acta 351 (2003) 133.
[71] C. Degueldre, D. Reed, A.J. Kropf, C. Mertz, J. Synchrotron. Rad. 11 (2004) 198.
[72] E.A. Ghabbour, G. Davis (Eds.), Humic Substances: Molecular Details and Applications in Land and Water Conservation, Taylor & Francis, Inc., New York, 2005.
[73] M.A. Vairavamurthy, D. Maletic, S. Wang, B. Manowitz, T. Eglinton, T. Lyons, Energy and Fuels 11 (1997) 546.
[74] S.C.B. Myeni, Soft X-ray spectroscopy and spectromicroscopy studies of organic molecules in the environment, in: P.A. Fentner, M.L. Rivers, N.C. Sturchio, S.R. Sutton (Eds.), Applications of Synchrotron Radiation in Low-temperature Geochemistry and Environmental Science, Mineralogical Society of America, Washington, DC, 2002, p. 485.
[75] U. Neuhäusler, H. Feng, K.W. Jones, J. Phys. IV France 104 (2003) 439.
[76] S. Beauchemin, D. Hesterberg, M. Beauchemin, Soil Sci. Soc. Am. J. 66 (2002) 83.
[77] J. Prietzel, J. Thieme, U. Neuhäusler, J. Susini, I. Kögel-Knabner, Eur. J. Soil. Sci. 54 (2003) 423.
[78] M.A. Denecke, C.M. Marquardt, J. Rothe, K. Dardenne, M.P. Jensen, J. Nucl. Sci. Technol. 3 (2002) 410.
[79] C.M. Marquardt, V. Pirlet, J.I. Kim, Wissenschaftliche Berichte Forschungszentrum Karlsruhe, vol. 6524, 2000, 45 pp.
[80] G. Martens, P. Rabe, N. Schwentner, A. Werner, Phys. Rev. Lett. 39 (1977) 1411.
[81] J. Rothe, M.A. Denecke, K. Dardenne, J. Colloid Interf. Sci. 231 (2000) 91.
[82] M. Plaschke, J. Rothe, T. Schäfer, M.A. Denecke, K. Dardenne, S. Pompe, K.-H. Heise, Colloid Surf. A 197 (2002).
[83] A.C. Scheinost, R. Kretzschmar, I. Christl, C. Jacobsen, Spec. Pub. – Roy. Soc. Chem. 273 (2002) 39.
[84] J. Thieme, C. Schmidt, G. Abbt-Braun, C. Specht, F.H. Frimmel, in: F.H. Frimmel, G. Abbt-Braun (Eds.), Refractory Organic Substances in the Environment, Wiley, New York, 2000.
[85] J. Rothe, M. Plaschke, M.A. Denecke, J. Phys. IV France 104 (2003).
[86] M. Plaschke, J. Rothe, M. Altmaier, M.A. Denecke, T. Fanghänel, J. Electron Spectrosc. Relat. Phenom. 148 (2005) 151.
[87] M. Plaschke, J. Rothe, M.A. Denecke, T. Fanghänel, J. Electron Spectrosc. Relat. Phenom. 135 (2004) 53.
[88] Z. Szabo, H. Moll, I. Grenthe, J. Chem. Soc., Dalton Trans. (2000) 3158.
[89] D.L. Clark, S.D. Conradson, S.A. Ekberg, N.J. Hess, D.R. Janecky, M.P. Neu, P.D. Palmer, C.D. Tait, New J. Chem. 20 (1996) 211.
[90] W. Runde, M.P. Neu, S.D. Reilly, in: D.T. Reed, S.B. Clark, L. Rao (Eds.), Actinide Speciation in High Ionic Strength Media, Kluwer Academic Press, New York, 1999, p. 141.
[91] D.L. Clark, D.E. Hobart, M.P. Neu, Chem. Rev. 95 (1995) 25.
[92] C. Spoetl, M. Unterwurzacher, A. Mangini, F.J. Longstaffe, J. Sediment Res. 72 (2002) 793.
[93] R.J. Reeder, M. Nugent, C.D. Tait, D.E. Morris, S.M. Heald, K.M. Beck, W.P. Hess, A. Lanzirotti, Geochim. Cosmochim. Acta 65 (2001) 3491.
[94] R.J. Reeder, M. Nugent, G.M. Lamble, C.D. Tait, D.E. Morris, Environ. Sci. Technol. 34 (2000) 638.
[95] N.C. Sturchio, M.R. Antonio, L. Soderholm, S.R. Sutton, J.C. Brannon, Science 281 (1998) 971.
[96] G. Geipel, T. Reich, V. Brendler, G. Bernhard, H. Nitsche, J. Nucl. Mater. 248 (1997) 408.
[97] S. Kelly, M.G. Newville, L. Cheng, K.M. Kemner, S.R. Sutton, P. Fentner, N.C. Sturchio, C. Spötl, Environ. Sci. Technol. 37 (2003) 1284.
[98] R.J. Reeder, M. Nugent, C.D. Tait, D.E. Morris, S.M. Heald, K.M. Beck, W.P. Hess, A. Lanzirotti, Geochim. Cosmochim. Acta 65 (2001) 3491.
[99] K.F. Hayes, A.L. Roe, G.E. Brown Jr., K.O. Hodgson, J.O. Leckie, G.A. Parks, Science 238 (1987) 51.
[100] C.J. Chrisholm-Brause, G.E. Brown Jr., G.A. Parks, Physica B, C 158 (1989) 646.
[101] C.J. Chrisholm-Brause, K.F. Hayes, A.L. Roe, G.E. Brown Jr., G.A. Parks, J.O. Leckie, Geochim. Cosmochim. Acta 54 (1990) 1897.
[102] A.J. Dent, J.D.F. Ramsay, W. Swanton, J. Colloid Interf. Sci. 150 (1992) 45.
[103] S.E. Fendorf, D.L. Sparks, G.M. Lamble, M.J. Kelley, Soil Sci. Soc. Am. J. 58 (1994) 1583.
[104] P.A. O'Day, G.A. Parks, G.E. Brown Jr., Clays Clay Miner. 42 (1994) 337.
[105] P.A. O'Day, G.E. Brown Jr., G.A. Parks, J. Colloid Interf. Sci. 165 (1994) 269.
[106] T. Reich, H. Moll, T. Arnold, M.A. Denecke, C. Hennig, G. Geipel, G. Bernhard, H. Nitsche, P.G. Allen, J.J. Bucher, N.M. Edelstein, D.K. Shuh, J. Electron Spectrosc. Relat. Phenom. 96 (1998) 237.
[107] E.A. Hudson, L.J. Terminello, B.E. Viani, M.A. Denecke, T. Reich, P.G. Allen, J.J. Bucher, D.K. Shuh, N.M. Edelstein, Clays Clay Miner. 47 (1999) 439.
[108] E.R. Sylwester, E.A. Hudson, P.G. Allen, Geochim. Cosmochim. Acta 64 (2000) 2431.
[109] K. Dardenne, T. Schäfer, M.A. Denecke, J. Rothe, J.I. Kim, Radiochim. Acta 89 (2001) 469.
[110] M.C. Hsiao, H.P. Wang, Y.L. Wei, J.E. Chang, C.J. Jou, J. Hazard Mater. 91 (2002) 301.
[111] J.R. Bargar, R. Reitmeyer, J.A. Davis, Environ. Sci. Technol. 33 (1999) 2481.
[112] L.N. Moyes, M.J. Jones, W.A. Reed, F.R. Livens, J.M. Charnock, J.F.W. Mosselmans, C. Hennig, D.J. Vaughan, R.A.D. Pattrick, Environ. Sci. Technol. 36 (2002) 179.
[113] D.H. Templeton, L.K. Templeton, Acta Cryst. A 38 (1982) 62.
[114] M.D. Crapper, Vacuum 45 (1994) 691.
[115] J.G. Catalano, T.P. Trainor, P.J. Eng, G.A. Waychunas, G.E. Brown, Geochim. Cosmochim. Acta 69 (2005) 3555.
[116] M.A. Denecke, K. Dardenne, P. Lindqvist-Reis, J. Rothe, Phys. Chem. Chem. Phys. 5 (2003) 939.
[117] J. Bruno, L. Duro, M. Grivé, Chem. Geol. 190 (2002) 371.
[118] G. Kamei, M.S. Mitsui, K. Futakuchi, S. Hashimoto, Y. Sakuramoto, J. Phys. Chem. Sol. 66 (2005) 612.
[119] K. Horie, H. Hidaka, Radiochim. Acta 92 (2004) 805.
[120] P. Kister, M. Cuney, V.N. Golubev, J.J. Royer, C.L.D. Veslud, J.C. Rippert, Comptes Rendus Geo. 336 (2004) 205.
[121] M. Fayek, S. Utsunomiya, R.C. Ewing, L.R. Riciputi, K.A. Jensen, Am. Min. 88 (2003) 1583.
[122] U. Noseck, T. Brasser, P. Rajlich, A. Laciok, M. Hercik, Radio. Chim. Acta 92 (2004) 797.

[123] M.A. Denecke, K. Janssens, K. Proost, J. Rothe, U. Noseck, Environ. Sci. Technol. 39 (2005) 2049.
[124] M.C. Duff, M. Newville, D.B. Hunter, P.M. Bertsch, S.R. Sutton, I.R. Triay, D.T. Vaniman, P. Eng, M.L. Rivers, J. Synchrotron. Rad. 6 (1999) 350.
[125] D.B. Hunter, P.M. Bertsch, J. Radioanal. Nucl. Chem. 234 (1998) 237.
[126] O.C. Lind, B. Salbu, K. Janssens, K. Proost, H. Dahlgaard, J. Environ. Rad. 81 (2005) 21.
[127] K. Janssens, K. Proost, G. Falkenberg, Spectrochim. Acta B 59 (2004) 1637.
[128] Z. Smit, K. Janssens, K. Proost, I. Langus, Nucl. Instr. Meth. Phys. Res. B 219–22 (2004) 35.
[129] Y. Dusausoy, N.E. Ghermani, R. Podor, M. Cuney, Euro. J. Min. 8 (1996) 667.
[130] R.H. Rundel, N.C. Baenzinger, A.S. Wilson, R.A. McDonald, J. Am. Chem. Soc. 70 (1948) 99.
[131] Actinide and Fission Product Partitioning and Transmutation, Status and Assessment Report, OECD Nuclear Energy Agency, Paris, 1999.
[132] K.L. Nash, in: K.A. Gschneidner Jr., L. Eyring, G.R. Choppin, G.H. Lander (Eds.), Handbook on the Physics and Chemistry of Rare Earth, Elsevier Science, Amsterdam, 1994.
[133] C. DenAuwer, M.C. Charbonnel, M.G.B. Drew, M. Grigoriev, M.J. Hudson, P.B. Iveson, C. Madic, M. Nierlich, M.T. Presson, R. Revel, M.L. Russell, P. Thuery, Inorg. Chem. 39 (2000) 1487.
[134] C. DenAuwer, C. Lecouteux, M.C. Charbonnel, C. Madic, R. Guillaumont, Polyhedron 16 (1997) 2233.
[135] M.P. Jensen, A.H. Bond, J. Am. Chem. Soc. 124 (2002) 9870.
[136] S. Tsushima, Y. Uchida, T. Reich, Chem. Phys. Lett. 357 (2002) 73.
[137] U. Wahlgren, H. Moll, I. Grenthe, B. Schimmelpfennig, L. Maron, V. Vallet, O. Gropen, J. Phys. Chem. A103 (1999) 8257.
[138] V. Vallet, H. Moll, U. Wahlgren, Z. Szabo, I. Grenthe, Inorg. Chem. 42 (2003) 1982.
[139] J.A. Greathouse, H.R. Stellalevinsohn, M.A. Denecke, A. Bauer, R.T. Pabalan, Clays Clay Miner. 53 (2005) 278.
[140] C. Madic, M.J. Hudson, J.O. Liljenzin, J.P. Glatz, R. Nannicini, A. Facchini, Z. Kolarik, R. Odoj, New partitioning techniques for minor actinides, EUR 19149, European Commission, Luxembourg, 2000.
[141] Z. Kolarik, U. Müllich, F. Gassner, Solvent Extr. Ion Exch. 17 (1999) 1155.
[142] M.A. Denecke, A. Rossberg, P.J. Panak, M. Weigl, B. Schimmelpfennig, A. Geist, Inorg. Chem., in press.
[143] A. Rossberg, A.C. Scheinost, Physica Scripta T115 (2005) 912.
[144] R. Ahlrichs, M. Bär, M. Häser, H. Horn, C. Kölmel, Chem. Phys. Lett. 162 (1989) 165.
[145] S. Colette, B. Amekraz, C. Madic, L. Berthon, G. Cote, C. Moulin, Inorg. Chem. 43 (2004) 6745.
[146] R.D. Deslattes, E.G.K.P. Indelicato Jr., L.D. Billy, E. Lindroth, J. Anton, Rev. Mod. Phys. 75 (2003) 35.
[147] P.B. Iveson, C. Riviere, D. Guillaneux, M. Nierlich, P. Thuéry, M. Ephritikhine, C. Madic, Chem. Commun. (2001) 1512.